Correspondence to:
J. P. A. Pitt,
jordan.pitt@adelaide.edu.au

Model Predictions of Wave Overwash Extent Into the Marginal Ice Zone

Jordan P. A. Pitt[1] , **Luke G. Bennetts[1]** , **Michael H. Meylan[2]** , **Robert A. Massom[3,4,5]** , and **Alessandro Toffoli[6]**

[1]School of Mathematical Sciences, University of Adelaide, Adelaide, SA, Australia, [2]School of Information and Physical Sciences, The University of Newcastle, Callaghan, NSW, Australia, [3]Australian Antarctic Division, Kingston, TAS, Australia, [4]Australian Antarctic Program Partnership, Institute for Marine and Antarctic Studies, University of Tasmania, Hobart, TAS, Australia, [5]The Australian Centre for Excellence in Antarctic Science, University of Tasmania, Hobart, TAS, Australia, [6]Department of Infrastructure Engineering, University of Melbourne, Parkville, VIC, Australia

Abstract In the marginal ice zone (MIZ), where ocean waves and sea ice interact, waves can produce flows of water across ice floe surfaces in a process known as wave overwash. Overwash potentially influences wave propagation characteristics, floe thermodynamics, and floe surface biological and chemical processes. However, the extent of the MIZ affected by overwash and its dependence on prevailing wave and ice conditions is unknown. In this paper, we propose a model of overwash extent caused by irregular incoming waves into a MIZ consisting of a random floe field. We validate the overwash extent model against laboratory experiments. We use the model to study mild to extreme incoming waves to floe field characteristics of the spring–summer ice retreat and autumn–winter ice advance and with compact ice edges. Overwash is typically predicted to extend a few kilometers and is generally greater for the autumn–winter advance than the spring–summer retreat. The model predictions provide a basis for improved understanding of the impacts of ocean waves on the ice cover. We also apply the model to incoming waves and a floe field with a diffuse ice edge representative of conditions during a field experiment, predicting overwash extents up to 16 km. During the field experiment, the wave and ice floe properties were intermittently monitored by a camera system, demonstrating how the sparse field data available on overwash can be advanced.

Plain Language Summary Wave overwash is the flow of water across the surface of a thin floating body due to passing waves. It is an important process in the marginal ice zone (MIZ) where sea ice floes and ocean waves interact. Overwash reduces the energy of ocean waves, removes snow from, and wets the sea ice surface, which can drive growth or melting. Water left on the sea ice surface can host organisms and affects chemical processes taking place there. Overwash is pervasive in laboratory experiments where it has been measured and studied. In contrast, there are few reports of overwash in the field and the extent of its occurrence has not been measured. We propose a model to predict the region of the MIZ in which overwash occurs. We use the model to compare overwash extents for MIZs associated with the spring–summer ice retreat and autumn–winter ice advance for calm to energetic wave conditions, including the conditions observed during a winter Antarctic icebreaker voyage. For field conditions, the model predicts that overwash typically extends at least several kilometers into the MIZ, indicating that it likely contributes to the ice edge evolution.

1. Introduction

The marginal ice zone (MIZ) is the highly dynamic outer band of the sea ice covered ocean in both polar regions, in which surface gravity waves and sea ice interact. The sea ice cover in the MIZ varies between regions (Weeks & Hilber, 2010) and depends on the season (Alberello et al., 2019; Doble, 2003; Hwang et al., 2017; Toyota et al., 2011) and synoptic conditions (Finocchio et al., 2020; Vichi et al., 2019). The ice cover comprises floating bodies of consolidated sea ice called floes (Armstrong & Roberts, 1956) separated by interstitial ice or open water. The concentration (fraction of ice-covered ocean surface in a unit area) of floes and interstitial ice is typically combined into a single ice concentration (Melsheimer & Spreen, 2019). Ice concentration typically increases with distance from the open (ice-free) ocean. The edge of the MIZ, adjacent to the open ocean, can be either compact (Massom et al., 2008) or diffuse (Massom & Stammerjohn, 2010) with bands of ice separated by open water being a common feature of diffuse ice edges (Wadhams, 1983). The ice cover in the MIZ can be broadly characterized as (i) pancake floes (Alberello et al., 2019; Doble, 2003; MIZEX Group, 1986; Rothrock &

Figure 1. Photo of pancake floes in the wake of the S.A. Agulhas II on its winter 2019 voyage. The wake is propagating to the right and water deposited on the floe surfaces by overwash can be seen behind the leading wave with some floes temporarily submerged.

Thorndike, 1984; Weeks & Ackley, 1982) or (ii) fragmented floes and brash ice (Collins et al., 2015; Frankenstein et al., 2001; Toyota et al., 2011). Type (i) MIZs are formed when the surface of the ocean freezes with waves preventing full consolidation of the sea ice cover (Wadhams et al., 1987), while driving collisions of adjacent floes resulting in their distinctive "pancake" shape (Shen et al., 2001; Weeks & Ackley, 1982). Type (i) MIZs are thus generally associated with the autumn and winter advance of sea ice. Type (ii) MIZs are produced by the breakup of large floes due to wave-induced flexural stresses (Kohout et al., 2016; Prinsenberg & Peterson, 2011). Type (ii) MIZs can occur year round but are particularly associated with the retreat of the ice cover in spring and summer.

Waves set each individual floe in the MIZ into motion, where the motion experienced by a particular floe depends both on its properties and those of the local wavefield. A floe sufficiently small relative to the local wavelength moves approximately in phase with the waves and does not disturb the surrounding wavefield other than to dissipate a small proportion of wave energy (Ardhuin et al., 2016; Squire et al., 1995). As the floe size relative to the local wavelength increases, the floe moves increasingly out of phase with the waves and begins to scatter wave energy in different directions (Bennetts & Williams, 2015; Meylan & Squire, 1994). Wave energy attenuates with distance from the open ocean into the MIZ due to an accumulation of scattering and dissipation (Squire, 2020), thus limiting the MIZ width and forming a coupled wave–floe interaction system. Short-period components of the wave spectrum attenuate quickly and penetrate only several kilometers into the MIZ, whereas long-period components attenuate slowly and can penetrate tens to hundreds of kilometers into the MIZ (Meylan et al., 2014; Squire & Moore, 1980). Therefore, the wave spectrum skews toward longer periods with increasing distance into the MIZ (Alberello et al., 2022).

In the scattering regime, where floe and wave motions are out of phase, water can flow across the surface of a floe in a process known as wave overwash (Massom, 1991; Massom et al., 1997, 1998), hereafter referred to as overwash. Overwash is a dynamic wave-driven process, distinct from flooding where floes become submerged due to mass added by snow or other floes (Wadhams et al., 1987). Figure 1 shows overwash of pancake floes by the wake of the S.A. Agulhas II during its winter 2019 voyage. The overwash produced by the wake deposited a significant amount of water on the floes, temporarily submerging some floes. The process of overwash is the same whether waves are produced by the ship as in Figure 1 and Dumas-Lefebvre and Dumont (2021) or are naturally occurring as is generally the case in the MIZ. While there are reports of overwash due to ocean waves in the MIZ (Massom, 1991; Massom et al., 1997, 1998), there has been no systematic study of overwash in the field. This is largely due to the challenge and difficulty of systematically measuring overwash, given that it predominantly occurs in the outermost region of the MIZ during large wave events.

Over the past 10 years, laboratory experiments have become a common approach to model wave–floe interactions and wave attenuation in the MIZ using either fresh water ice (Alberello et al., 2021; Dolatshah et al., 2018; Yiew et al., 2019), model ice (Cheng et al., 2019; Passerotti et al., 2022), or most often, artificial floes (Bai et al., 2017; Bennetts et al., 2015; Bennetts & Williams, 2015; Huang et al., 2022; Meylan, Yiew, et al., 2015; Montiel, Bonnefoy, et al., 2013; Nelli et al., 2017; Sree et al., 2018, 2020; Toffoli et al., 2015; Toffoli et al., 2022; Yiew et al., 2017). In contrast to the scarce reporting in the field, overwash is a pervasive feature of laboratory experiments. In laboratory experiments, overwash occurs even for relatively small steepness waves, which would usually be considered linear, due to the small freeboard of floes (Skene et al., 2015). Analysis of experimental data has given strong evidence that overwash causes wave energy dissipation and hence increases attenuation (Bennetts et al., 2015; Bennetts & Williams, 2015; Nelli et al., 2017; Toffoli et al., 2015, 2022). Overwash has also been associated with accelerated melt and breaking of the edge of model ice (Passerotti et al., 2022). The laboratory experiments have motivated the development of overwash models (Skene & Bennetts, 2021; Skene et al., 2015, 2018) and simulations of overwash using computational fluid dynamics software (Huang et al., 2019; Huang & Thomas, 2019; Nelli et al., 2020; Tran-Duc et al., 2020). The models and simulations of overwash show promising agreement with measurements in terms of overwash properties and wave attenuation due to overwash, but are restricted to regular incoming waves and single floes at present.
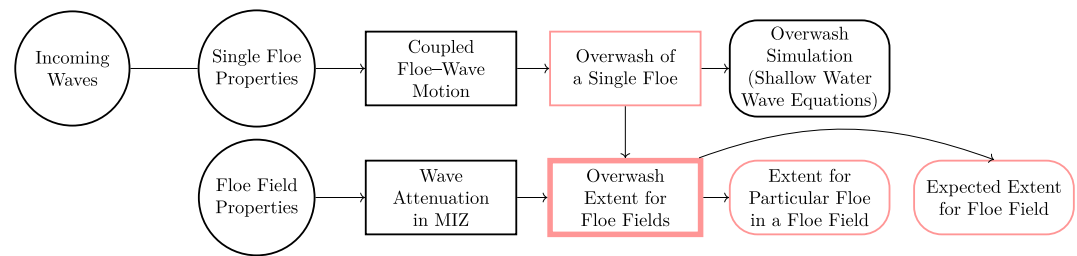
Figure 2. Overview of model, showing inputs (◯), sub-models (▭), main model (▬), outputs (◯), and their relationships (⟶) with novel contributions highlighted in pink.

In this article, we build on recent progress in modeling overwash of a single floe by regular incoming waves (Skene et al., 2015) to develop a stochastic model of overwash extent in the MIZ caused by irregular incoming waves. The model incorporates the ice conditions, described by an ice thickness, a floe concentration, and a floe size distribution (FSD). The model includes wave attenuation due to scattering by the floes and an empirical model for wave dissipation in the MIZ. Thus, the model is capable of predicting the occurrence and extent of overwash into the MIZ for given wave and ice conditions. We validate the model using a laboratory experiment, for which overwash was previously reported but not quantified (Bennetts & Williams, 2015). We use the model to investigate the effect of calm and energetic seas in the Southern Ocean (Young et al., 2020) for the Antarctic MIZ when it is Type (i) comprising pancake floes (Alberello et al., 2019) or Type (ii) comprising fragmented floes (Toyota et al., 2011). Finally, we use the model to predict the region of overwash for inputs that replicate the wave and ice conditions during a field experiment in the Antarctic MIZ, where stereo-camera images of waves and ice floes were captured (Alberello et al., 2019, 2022; Vichi et al., 2019).

2. Model Overview

Our model takes inputs (circles) describing wave and ice properties and uses multiple sub-models (rectangles) to produce predictions of overwash extent in the MIZ (Figure 2). Predictions of overwash extent for the MIZ (second row), described as a random field of floes, are based on predictions of the overwash of a single floe with known properties by incoming waves under time-harmonic conditions (first row). Incoming irregular waves are specified using a wave spectrum (Section 3.1.1), describing an ensemble of possible incoming waves. For the ensemble of incoming waves, the ensemble of time-harmonic coupled floe–wave motions is determined. From the ensemble of time-harmonic coupled floe–wave motions, the ensemble average frequency of overwash events of the single floe is calculated. The ensemble average frequency of overwash events of the single floe is then used to determine if the floe is overwashing, producing the nonlinear (amplitude-dependent), stochastic sub-model for overwash of a single floe.

The overwash of a single floe under time-harmonic conditions is extended to a field of floes (second row), assuming no floe–floe interactions (collisions or rafting). The floe fields add an extra layer to the stochastic nature of the model as they are described by an ensemble of possible floe fields for a given FSD (Section 3.2.1) (Rothrock & Thorndike, 1984). The ensemble average attenuation of irregular waves due to the ensemble of floe fields encountered is calculated by the linear wave attenuation sub-model (Bennetts et al., 2007; Meylan et al., 2014). The attenuated irregular waves in the floe field are used to determine the overwash event frequency of individual floes in the floe field, thereby generating a nonlinear, stochastic model of overwash extent in the MIZ. Two outputs are used to measure extent of overwash, that is, the distance from the boundary of the floe field until overwash events for individual floes are sufficiently rare. The first gives the maximum distance a particular floe of known properties can be placed into a random floe field and be overwashed. The second gives the maximum distance most floes in the random floe field will be overwashed using the expected value of overwash event frequency for the random floe field.
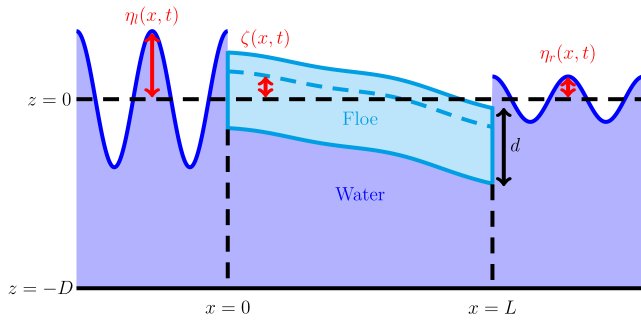
Figure 3. Snapshot of the time-harmonic coupled floe–wave motion (Equation 4) in response to an incoming regular wave (from the left).

3. Model Components

3.1. Overwash of a Single Floe

3.1.1. Incoming Waves

We describe irregular incoming waves using a large number N of regular wave components, which are equally spaced in some fixed frequency range $[\omega_1, \omega_N]$. Each regular wave component has a prescribed angular frequency ω_n, a phase θ_n selected randomly from uniformly distribution over $[0, 2\pi)$, and an amplitude A_n selected randomly from a Rayleigh distribution (Holthuijsen, 2010). The mean value of the Rayleigh distribution is $\sqrt{2S(\omega_n)\Delta\omega}$, where $S(\omega)$ is the one-dimensional energy density spectrum and $\Delta\omega$ is the uniform frequency spacing.

For a given spectrum, S, the free surface of the water at a horizontal location x and time t for the incoming waves is

$$\eta_I(x, t) = \sum_{n=1}^{N} A_n e^{i(k_n x - \omega_n t + \theta_n)}. \tag{1}$$

The wavenumber k_n satisfies the linear, finite-depth dispersion relation with a depth of 1,000 m that approximates deep water conditions, that is, $k_n \approx \omega_n^2 / g$, where $g = 9.81\ \mathrm{m\,s^{-2}}$ is the acceleration due to gravity.

The spectrum we use in Sections 3–5 is the JONSWAP spectrum (Hasselmann et al., 1973), defined by

$$S_{jp}(\omega; \tau_p) = 2\pi \beta g^2 \omega^{-5} \exp\left(-\frac{5}{4}\left(\frac{\omega}{\omega_p}\right)^{-4}\right) \gamma^{\Lambda} \tag{2a}$$

where

$$\gamma = 3.3, \quad \Lambda = \exp\left(-\frac{\left(\frac{\omega}{\omega_p} - 1\right)^2}{2\left(\sigma\left(\frac{\omega}{\omega_p}\right)\right)^2}\right) \quad \text{and} \quad \sigma(x) = \begin{cases} 0.07 & x < 1 \\ 0.09 & \text{otherwise.} \end{cases} \tag{2b}$$

The spectrum is parameterized by a peak period τ_p (peak frequency $\omega_p = 2\pi/\tau_p$) where it attains its maximum value. The spectrum is also modified by the "Phillips" parameter β.

The numerical results in Sections 4–5 are used to investigate how the significant wave height, H_s, and the peak period, τ_p, affect overwash extent. To facilitate the investigation, we normalize the JONSWAP spectrum (Equation 2a) to

$$\tilde{S}_{jp}(\omega; \tau_p, H_s) = \frac{H_s^2}{16} \frac{S_{jp}(\omega; \tau_p)}{\int_0^\infty S_{jp}(\omega; \tau_p)\,d\omega}, \tag{3}$$

which fixes the spectral shape given by γ and σ and replaces the scale dependence on β with H_s.

3.1.2. Coupled Floe–Wave Motions

We produce a two-dimensional coupled floe–wave motion model for incoming irregular waves by applying linear superposition to a regular wave (single frequency) version of the time-harmonic model. The regular wave model is described first and then extended to the irregular wave model. We subsequently regard the regular wave model as a degenerate case of the irregular wave model.

The horizontal axis (x) has its origin at the left edge of the floe, and the vertical axis (z) has its origin at the still water line (Figure 3). The water has constant density ρ, where, unless otherwise stated, $\rho = 1{,}025\ \mathrm{kg\,m^{-3}}$ and finite-depth water that approximates the deep water conditions (depth is 1,000 m).

The floe has length L, thickness d, and density ρ' and hence Archimedean draught $d_d = (\rho'/\rho)\,d$ and freeboard $d_f = d - d_d$. The elastic response of the floe is governed by a Young's modulus E, which controls the stiffness,
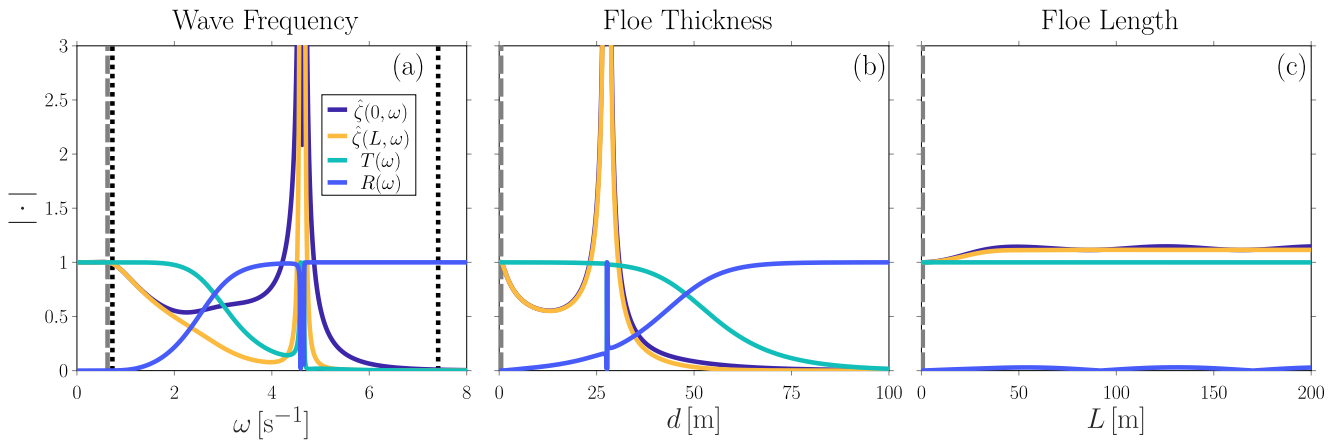
Figure 4. Dependence of the absolute value of transmission, reflection, and plate edge coefficients in Equation 4 on (a) wave frequency ω, (b) floe thickness d, and (c) floe length L. The fixed values (a) $\tau = 10$ s, (b) $d = 0.7$ m, and (c) $L = 0.5$ m are highlighted (━ ━). In (a), the short- and long-wave limits are indicated (▪▪▪▪).

and a Poisson ratio ν, which describes expansion perpendicular to the direction in which force is applied. We use the standard values for sea ice, $E = 6$ GPa, $\nu = 0.3$, and $\rho' = 920$ kg m^{-3} (Bennetts & Squire, 2012a; Timco & Weeks, 2010).

Linear potential flow theory governs the motion of the water surrounding and under the floe. The water surrounding the floe has free surface $z = \eta(x, t)$ ($x < 0$ and $x > L$). We use the Kirchoff–Love thin plate theory to model the motion of the floe in terms of the vertical displacement of its neutral plane, $\zeta(x, t)$ ($0 < x < L$), so that the bottom of the floe is at $z = \zeta(x, t) - d_d$ and the top of the floe is $z = d_f + \zeta(x, t)$. The floe displacement is a combination of rigid-body motions, heave and pitch, and elastic motions (Montiel, Bennetts, et al., 2013).

We obtain the time-harmonic wavefield and floe motions (Figure 3) in response to an incoming regular wave with angular frequency ω and amplitude A using the variational method of Bennetts et al. (2007). The wavefield to the left of the floe, $\eta(x, t) \equiv \eta_l(x, t)$ ($x < 0$), is a combination of the incoming regular wave and a regular reflected wave, while the wavefield on the right, $\eta(x, t) \equiv \eta_r(x, t)$ ($x > L$), is the transmitted regular wave. The time-harmonic solutions are

$$\eta_l(x, t) = A \operatorname{Re}\left\{\left(e^{ikx} + R(\omega)e^{-ikx}\right)e^{-i\omega t}\right\} \tag{4a}$$

$$\eta_r(x, t) = A \operatorname{Re}\left\{T(\omega)e^{ik(x-d)}e^{-i\omega t}\right\} \tag{4b}$$

$$\zeta(x, t) = A \operatorname{Re}\left\{\hat{\zeta}(x, \omega)e^{-i\omega t}\right\}, \tag{4c}$$

where $R(\omega)$ and $T(\omega)$ are complex-valued reflection and transmission coefficients, respectively, and $\hat{\zeta}(x, \omega)$ is the complex-valued floe displacement profile. Evanescent modes, which decay exponentially away from the floe edges, are included in the calculations of $R(\omega)$, $T(\omega)$ and $\hat{\zeta}$, but are neglected in Equations 4a and 4b, following Skene et al. (2015).

The reflection and transmission coefficients and the displacement profile at the floe edges depend on the incoming ω, the floe thickness d, and the floe length L (Figure 4). The dependence on incoming ω is demonstrated for a typical pancake floe (Figure 4a). The influence of the floe thickness (Figure 4b) and length (Figure 4c) is shown for a period comparable to peak periods in the Southern Ocean (Young et al., 2020). We describe the dependence of the wave–floe motion coefficients by the relative size of the incoming wavelength $\lambda = 2\pi/k$ to the floe thickness and floe length (Bennetts & Squire, 2012b; Meylan & Squire, 1994). The dependence is produced by the flexural-gravity wave induced in the coupled floe–water motions as explained by Meylan and Squire (1994). The system conserves energy, so that $|R(\omega)|^2 + |T(\omega)|^2 = 1$, and hence, an increase in reflected wave energy decreases transmitted wave energy and an increase in transmitted wave energy decreases reflected wave energy. When the wavelength is short compared to the floe thickness and length (high frequencies), then most of the incoming wave energy is reflected and the floe is essentially still, so that $|R(\omega)| \approx 1$ and $|\hat{\zeta}(x, \omega)| \approx 0$ with conservation ensuring that $|T(\omega)| \approx 0$. When the wavelength is long compared to the floe thickness and length (low frequencies), then

most incoming wave energy is transmitted and the floe moves in phase with the waves, so that $|T(\omega)| \approx 1$ and $|\hat{\zeta}(x, \omega)| \approx 1$ with conservation ensuring that $|R(\omega)| \approx 0$. Using a tolerance of 1% on the asymptotic values for the chosen floe, the long-wave regime occurs when $\omega < 0.7$ s^{-1} and $\lambda > 162\ d = 116\ L$, while the short-wave regime occurs when $\omega > 7.4$ s^{-1} and $\lambda < 1.5\ d = 1.1\ L$. The coupled floe–wave motion transitions between these two regimes as ω and d increase with some resonances apparent (Lever et al., 1988; Meylan & Squire, 1994). Increasing floe length also increases reflection, particularly when L is small. As L increases further, there is no overall trend as resonance effects dominate, producing consistent oscillations in coefficient values for large floe lengths (Figure 4b). We demonstrate in Section 4 that resonance effects average out for irregular waves leaving only the overall trends with respect to long and short wavelengths

The coupled floe–wave motions for an irregular incident wave are calculated as the linear superposition for the regular wave components, $\omega_1, \ldots, \omega_N$, similar to Equation 1. For each ω_n, the reflection, transmission, and floe displacement profile coefficients are calculated as described above. Since the problem is linear, for an incoming wave spectrum S, the wave spectra of the left (η_l) and right (η_r) of the floe at ω_n (Holthuijsen, 2010) are

$$S_{\eta,l}(\omega_n) = |1 + R(\omega_n)|^2\, S(\omega_n), \quad S_{\eta,r}(\omega_n) = |T(\omega_n)|^2\, S(\omega_n) \tag{5}$$

and the spectrum of floe displacement profile (ζ) is

$$S_\zeta(\omega_n, x) = \left|\hat{\zeta}(x, \omega_n)\right|^2 S(\omega_n). \tag{6}$$

The spectra (Equations 5 and 6) act as inputs to the overwash of a single floe model.

3.1.3. Overwash of a Single Floe

Overwash is generated when either floe edge moves below the surrounding water surface. Thus, an overwash event at time t occurs if either $\psi_l(t) = \eta_l(0, t) - \zeta(0, t)$ or $\psi_r(t) = \eta_r(d, t) - \zeta(L, t)$ are greater than the equilibrium freeboard, d_f. From Equations 5 and 6, the spectra describing ψ_l and ψ_r for each ω_n are, respectively,

$$S_l(\omega_n) = \left|1 + R(\omega_n) - \hat{\zeta}(0, \omega_n)\right|^2 S(\omega_n) \quad \text{and} \quad S_r(\omega_n) = \left|T(\omega_n) - \hat{\zeta}(d, \omega_n)\right|^2 S(\omega_n). \tag{7}$$

The spectra define ensembles of possible time series, where each realization is given by sampling the associated distributions of phases and amplitudes of the regular wave components. From the respective edge spectra (Equation 7), the ensemble average of the time between overwash events is (Rice, 1945)

$$\overline{\tau}_E(d_f) = \exp\left(\frac{d_f^2}{2m_0}\right)\sqrt{\frac{m_0}{m_2}} \quad \text{where} \quad m_j = \int_0^\infty \omega^j S_E\left(\omega^j\right) d\omega \quad (j = 0, 2), \tag{8}$$

for the left edge ($E = l$) and the right edge ($E = r$). The spectral moments m_j are calculated by quadrature using $\omega_1, \ldots, \omega_N$ as the quadrature points. Additionally, ω_1 and ω_N are chosen so that $S(\omega_1)$ and $S(\omega_N)$ are very small to ensure that the integrals are well approximated. We added a further height tolerance of ϵ, so that the mean time between overwash events at the left and right edges is $\overline{\tau}_l(d_f + \epsilon)$ and $\overline{\tau}_r(d_f + \epsilon)$, respectively. The value $\epsilon = 0.001$ m is used in the results presented in Sections 4. We provide a consistent measure of the prevalence of overwash events for a variety of incoming waves by defining the relative frequency of overwash events

$$f_o = \max\left\{\frac{\overline{\tau}_I(0)}{\overline{\tau}_l(d_f + \epsilon)}, \frac{\overline{\tau}_I(0)}{\overline{\tau}_r(d_f + \epsilon)}\right\}. \tag{9}$$

In Equation 9, $\overline{\tau}_I(0)$ is the mean wave period for the incoming spectrum S calculated using Equation 8. The relative frequency of overwash events is the maximum of the relative overwash event frequency at the left and right edges of the floe, since overwash events can occur at either edge. The floe is judged to experience overwash using Equation 9 if $f_o > f_{tol}$ where f_{tol} is a chosen threshold for relative frequency of overwash events. In Sections 4 and 5, we use $f_{tol} = 0.05$, so that a floe is determined to be overwashed when on average at least one overwash event occurs over 20 mean periods.

For regular waves

$$\psi_l(t) = A\operatorname{Re}\left\{\left(1 + R(\omega) - \hat{\zeta}(0, \omega)\right) e^{-i\omega t}\right\} \quad \text{and} \quad \psi_r(t) = A\operatorname{Re}\left\{\left(T(\omega) - \hat{\zeta}(L, \omega)\right) e^{-i\omega t}\right\}.$$
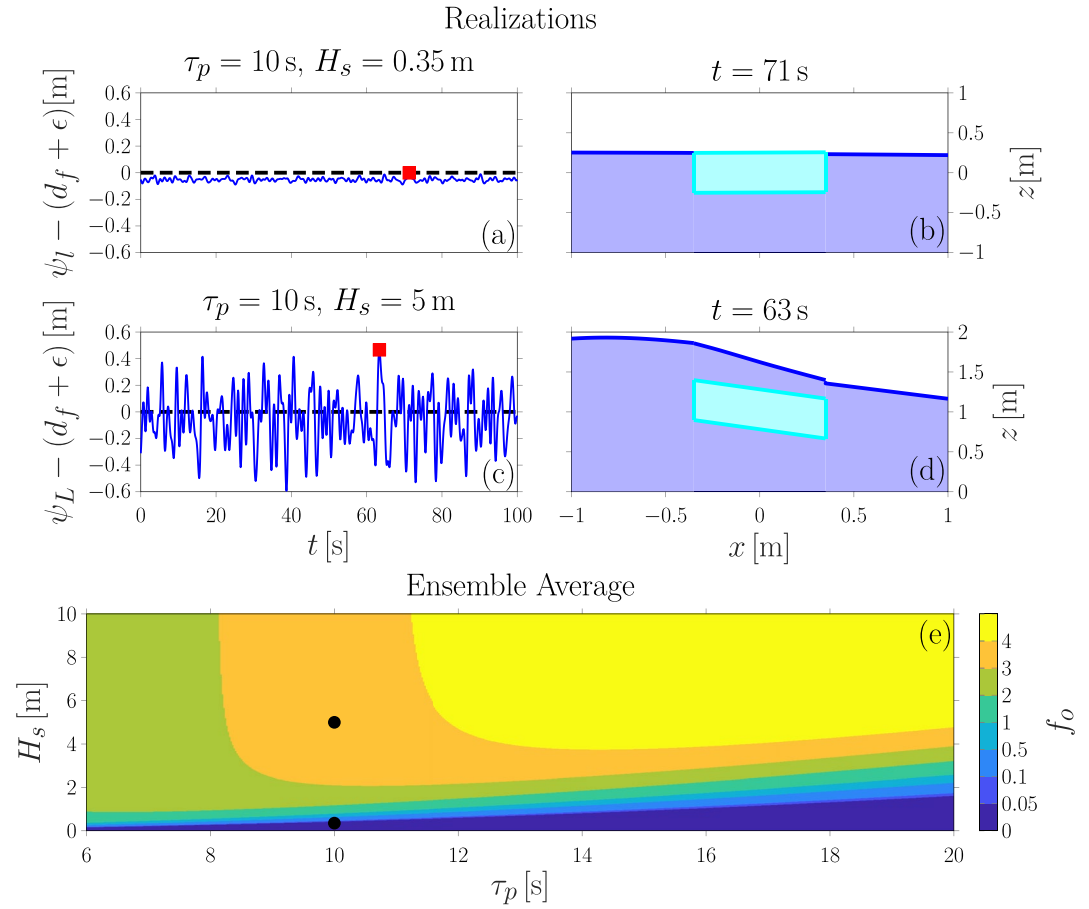
Figure 5. Comparison of (a–d) deterministic simulations of individual realizations of the spectra described by Equation 3 and (e) ensemble averages predictions of overwash event frequency for a mean length pancake floe ($L = 0.7$ m, $d = 0.5$ m). The deterministic simulations are shown as (a and c) time series of the left wavefield relative to the top left corner of the floe and (b and d) snapshots of the simulation at the highlighted time (■). The simulations show (a and b) nonoverwashing and (c and d) overwashing examples with their respective ensemble average of overwash event frequency shown (●) in (e).

Therefore, the mean time between overwash events (waves above $d_f + \epsilon$ at the floe edges) is

$$\overline{\tau}_l(d_f + \epsilon) = \begin{cases} \tau & \text{if } A|1 + R(\omega) - \hat{\zeta}(0,\omega)| > d_f + \epsilon \\ 0 & \text{otherwise} \end{cases}$$

$$\text{and} \quad \overline{\tau}_r(d_f + \epsilon) = \begin{cases} \tau & \text{if } A|T(\omega) - \hat{\zeta}(L,\omega)| > d_f + \epsilon \\ 0 & \text{otherwise,} \end{cases}$$

at the left and right edges, respectively. Consequently, the relative frequency of overwash events for regular waves is $f_o = 1$ when $A|1 + R(\omega) - \hat{\zeta}(0,\omega)| > d_f + \epsilon$ or $A|T(\omega) - \hat{\zeta}(L,\omega)| > d_f + \epsilon$, otherwise $f_o = 0$.

The behavior of overwash for a floe can also be determined by simulations of individual realizations of the incoming spectrum (process described in Appendix A). For a typical pancake floe, a realization of the spectrum (Equation 3) with $H_s = 0.35$ m (Figure 5a) has no overwash events ($\psi_l - (d_f + \epsilon) < 0$) as shown in the snapshot for maximum $\psi_l - (d_f + \epsilon)$ (Figure 5b). Thus, for the realization with $H_s = 0.35$ m, the relative overwash event frequency is zero. Overwash events occur frequently for the realization with $H_s = 5$ m (Figure 5c) with a relative overwash event frequency for the realization of 5.3, that is, just over five overwash events per mean wave period. The snapshot at the maximum (Figure 5d) shows overwash being forced at both the left and right edges of the

floe, completely submerging the floe. While overwash is generated at the right edge with an overwash event frequency of 3.5, more water is pushed onto the floe at the left edge so that it is the largest source of overwash.

The behavior of overwash for the realizations compares well to the prediction of overwash for the ensemble (Figure 5e). For the incoming spectrum with $H_s = 0.35$, the ensemble average is $f_o = 0.003 \ll f_{tol} = 0.05$. Therefore, overwash events are rare for the ensemble of incoming waves described by this spectrum. The ensemble average of relative overwash event frequency, f_o, compares well with the realization in which the relative overwash event frequency is zero (Figure 5a). In contrast, the incoming spectrum with $H_s = 5$ m has $f_o = 3.5 \gg f_{tol}$, so there are approximately three to four overwash events every mean period on average. The relative overwash event frequency of the ensemble is comparable to the relative overwash event frequency of 5.3 for the realization (Figure 5c), in which overwash events are frequent. Although the dependence of the wave and floe displacement coefficients on ω indicates the presence of resonance effects in Figure 3, the f_o contours Figure 5e are smooth and there are no anomalous behaviors for particular τ_p. Thus, resonance effects are not apparent in the ensemble average overwash predictions.

3.2. Overwash Extent of Floe Fields

3.2.1. Floe Field Properties

We assume a floe field composed of separated free-floating floes with no floe–floe interactions. The floe field is defined by a constant ice thickness and floe concentration and a prescribed FSD. For the investigation in Section 5, we chose ice thickness and floe concentration to be constant for simplicity, not due to limitations in the model. In Section 5.3, we relax the constant floe concentration restriction to match floe concentration variations in an observed MIZ.

The FSD is defined by the exceedance probability distribution $P^*(L)$, which gives the probability of finding a floe greater than length L in the floe field. We used a split power law FSD based on FSD observations in the MIZ (Alberello et al., 2019; Toyota et al., 2011). The exceedance probability given by a split power law is

$$P^*(L) = \begin{cases} 1 & \text{if} \quad L < L_{\min} \\ (1-\alpha)\,\beta_1\,L^{-\gamma_1} & \text{if} \quad L_{\min} \leq L \leq L_{crit} \\ \alpha\beta_2\,L^{-\gamma_2} & \text{if} \quad L_{crit} < L, \end{cases} \tag{10a}$$

where the parameters

$$\beta_1 = \frac{1}{L_{\min}^{-\gamma_1} - L_{crit}^{-\gamma_1}}, \quad \beta_2 = \frac{1}{L_{crit}^{-\gamma_2}} \quad \text{and} \quad \alpha = \left(1 + \frac{\beta_2 \gamma_2 L_{crit}^{-\gamma_2-1}}{\beta_1 \gamma_1 L_{crit}^{-\gamma_1-1}}\right)^{-1} \tag{10b}$$

ensure $P^*(L_{\min}) = 1$ and that the probability distribution is continuous at L_{crit} where the two power laws intersect. The parameters γ_1, γ_2, and L_{crit} are obtained by fitting floe size data, while $L_{\min}$ is the smallest measurable floe size.

For computations, a finite number of floe lengths, L_1, ..., L_M, are used. We used floe lengths, which were uniformly spaced, that is, $\Delta L = L_{m+1} - L_m$ was fixed for all $m = 1$, ..., $M - 1$. The exceedance probability P^* produces a probability distribution

$$p(L_m) = P^*(L_m - \Delta L/2) - P^*(L_m + \Delta L/2) \tag{11}$$

for the finite number of floe lengths, called the discrete FSD. This probability distribution results in all floes of length $L_m - \Delta L/2 \leq L \leq L_m + \Delta L/2$ in the continuous FSD being represented by a floe of length L_m in the discrete FSD.

The discrete FSD represents an ensemble of possible floe fields where each realization is generated by repeated sampling of the probability distribution (Equation 11). The resultant realization of the floe field will have a number of floes of length L_m, $N_f(L_m)$ and the proportion of $N_f(L_m)$ to the total number of floes will approach $p(L_m)$ as the total number of floes increases. A field of floes with a fixed floe concentration c_f over a distance x will

cover a distance of $c_f x$ when placed end to end. For a floe field described by the FSD (Equation 11), the expected number of floes covering a total end to end distance of $c_f x$ is $c_f x / \overline{L}$ where $\overline{L}$ is the mean floe size in the FSD.

Pancake and fragmented floe fields, representative of the MIZ in autumn–winter and spring–summer, respectively, will be investigated in Section 5. The FSD of a pancake floe field in an Antarctic MIZ was measured by Alberello et al. (2019), who found the FSD values $\gamma_1 = 1.1$, $\gamma_2 = 9.4$, $L_{crit} = 3.15$ m, and $L_{min} = 0.25$ m for Equation 10. The sea ice floe concentration was $c_f \approx 0.6$ throughout the measurement period. The thickness of pancake ice was not measured by Alberello et al. (2019), but is typically in the range of 0.1–1 m (Wadhams et al., 2018; Worby et al., 1996) and thus we take $d = 0.5$ m as the constant thickness for a pancake floe field. The floe field generated by a fragmented ice cover in the Weddell Sea was measured by Toyota et al. (2011), who found FSD values of $\gamma_1 = 1.39$, $\gamma_2 = 5.18$, $L_{crit} = 30$ m, and $L_{min} = 2$ m for Equation 10. The ice concentration varied in the range $c_i = 0.3–1$, and therefore, we use a floe concentration $c_f = 0.6$ for the fragmented floe field, making it consistent with the pancake floe field. The 95% confidence interval for the thickness of the floes was measured as 1.08 ± 1.07 m, and the mean thickness $d = 1.08$ m will be taken as the constant thickness for fragmented floe fields.

3.2.2. Wave Attenuation in the MIZ

We model the attenuation of the initial spectrum in the open ocean $S(\omega, 0)$, as it propagates over a distance x into the MIZ using a function $\mathcal{T}(\omega, x)$ so that

$$S(\omega, x) = \mathcal{T}(\omega, x)S(\omega, 0). \tag{12}$$

The attenuation function is expressed as the product $\mathcal{T}(\omega, x) = \mathcal{T}_{scat}(\omega, x)\mathcal{T}_{diss}(\omega, x)$, where $\mathcal{T}_{scat}(\omega, x)$ represents wave attenuation due to scattering and $\mathcal{T}_{diss}(\omega, x)$ represents attenuation due to dissipative effects. Attenuation due to scattering is produced by an accumulation of partial transmissions of wave energy and incoherent multiple scatterings (Bennetts & Squire, 2012b). Thus, attenuation due to scattering depends on the coupled floe–wave motions (modeled using Section 3.1.2) of all floes encountered by the incoming waves, which is determined by the FSD. The attenuation due to dissipation is generated by viscous processes in the interaction between individual floes and ocean waves, such as underside friction and overwash, as well as from multiple floe interactions such as collisions. Many models exist for attenuation due to dissipation (Meylan & Bennetts, 2018), but there is little consensus on them (Squire, 2020). Therefore, we use an empirical model for dissipation (Meylan et al., 2014), which accounts for the measured aggregate attenuation due to these viscous processes. The empirical model depends only on ω and x and not the ice properties.

Attenuation due to scattering varies according to the realization of the discrete FSD. To produce $\mathcal{T}_{scat}(\omega, x)$, we use the ensemble average of attenuation due to all realizations of the discrete FSD with a floe concentration c_f over a distance x. An individual floe of length L_m transmits a spectrum, which is attenuated by $|T(\omega, L_m)|^2$ due to scattering. Given a floe concentration c_f, a floe of length L_m occurs on average $q_m = p(L_m) c_f x / \overline{L}$ times over the distance x, where $\overline{L}$ is the average floe length for the FSD. The average attenuation in the ensemble described by the discrete FSD is then

$$\mathcal{T}_{scat}(\omega, x) = \prod_{m=1}^{M} \left(|T(\omega, d_m)|^2 \right)^{q_m}. \tag{13}$$

For a deterministic floe field (as in Section 4), the number of floes and floe lengths over the distance x is known. When the floe field is deterministic, the known counts of the respective floe lengths replace the exponent q_m.

Meylan et al. (2014) derived an empirical model for attenuation over distance based on measurements in an Antarctic MIZ. The relatively large wavelengths as compared to floe lengths in the study area suggest that scattering was negligible, and hence, dissipation was the dominant source of measured attenuation (Squire, 2020). The empirical model has been found to agree with measurements of attenuation in different wave and ice conditions (Meylan et al., 2018). The empirical dissipation attenuation model is

$$\mathcal{T}_{diss}(\omega, x) = e^{-\left(a_1 \left(\frac{\omega}{2\pi} \right)^2 + a_2 \left(\frac{\omega}{2\pi} \right)^4 \right) x}, \tag{14}$$
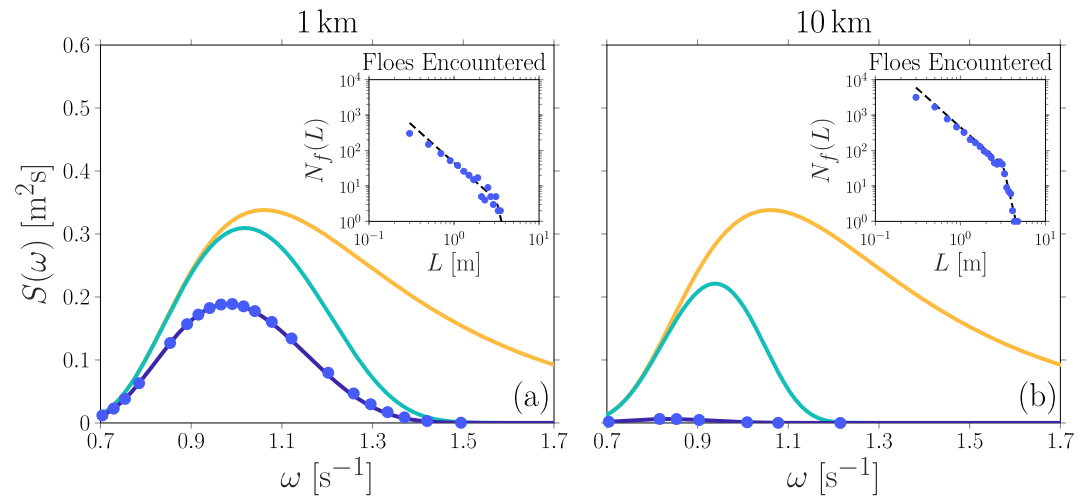
Figure 6. Attenuation of an example JONSWAP spectrum (Equation 3 with $H_s = 2$ m and $\tau_p = 6$ s, ■) through the pancake floe field with the ensemble average spectrum with (■) and without (■) $\mathcal{T}_{diss}$ and the attenuated spectrum after passing through a realization of the discrete FSD (●) over distances of (a) 1 km and (b) 10 km. The inset shows the respective count of the number of floes encountered $N_f(L)$ for each floe length L in the sample from the discrete FSD (●) (which produces the corresponding attenuated spectrum) compared to the underlying discrete FSD multiplied by the expected number of floes $\left(c_f x / \overline{L} \right)$ (■ ■).

with $a_1 = 2.12 \times 10^{-3}$ s^2 m^{-1} and $a_2 = 4.59 \times 10^{-2}$ s^4 m^{-1}. The proposed dependence of $\mathcal{T}_{diss}$ on the ice concentration (Bennetts et al., 2017) has not yet received supporting evidence, and thus, we omit it from the model for simplicity.

Combining the dissipation and scattering attenuation as in Equation 12 produces the modeled attenuation of the spectrum in a pancake floe field (Figure 6). Scattering dominates attenuation when wavelengths are compared to floe lengths (Bennetts & Williams, 2015; Squire et al., 1995), which is the high-frequency (short-period) regime $\omega > 1.4$ s^{-1} for the pancake floe field. However, the peak frequency of the incoming spectrum, $\omega_p = 0.79$ s^{-1}, is below the high-frequency regime and so dissipation dominates attenuation for the incoming spectrum. The attenuation reduces H_s by 24% after 1 km and by 38% after 10 km. The reduction in the significant wave height produced by the attenuation model (Equation 12) is greater than the 12% reduction over roughly 15 km observed by Alberello et al. (2022), which is attributed to local wave generation by winds in the MIZ and the changing wave conditions during those measurements.

The preferential attenuation of higher frequency waves results in a gradual increase in peak period, τ_p, as the spectrum propagates through the floe field. The ensemble average attenuated spectrum (Equation 13) and the attenuated spectrum of the realization are almost identical due to the dominance of $\mathcal{T}_{diss}$ as well as the proximity of the floe counts in the realization to the underlying probability distribution. The realization and the ensemble average attenuated spectra do not demonstrate resonance effects from the coupled–floe wave motions as they are smooth and lack the pronounced peaks seen in Figure 4.

3.2.3. Overwash Extent

We use the ensemble of floe fields described by the FSD and the attenuation function (Equation 12) to produce an ensemble average attenuated spectrum at some distance x into the floe field $S(\omega, x)$. We then use the ensemble of irregular waves described by the attenuated spectrum $S(\omega, x)$ to determine the ensemble average overwash event frequency for a given floe at that distance x into the floe field. To quantify the extent of overwash into a floe field, we employ two measures of overwash extent.

The first measure provides the overwash extent for a floe of length L. For this floe, the relative overwash event frequency at x is $f_o(x; L)$. For the chosen floe, the maximum extent X_L is the largest distance x such that

$$f_o \left(x; L, \underbrace{\{d, L_{crit}, L_{min}, \gamma_1, \gamma_2\}}_{\text{floe field}}, \underbrace{\{H_s, \tau_p\}}_{\text{wave}} \right) > f_{tol},$$

where the implicit dependencies on the floe field (Section 3.2.1) and incoming wave properties (Section 3.1.1) have been made explicit. Thus, X_L is the largest distance the floe with known length is predicted to be overwashed by the single floe overwash model.

The second measure yields the expected overwash extent for all floes in the FSD at a set distance x. It uses the expected relative frequency of overwash events for all floes at x, which is

$$\overline{f}_o(x) = \sum_{m=1}^{M} f_o(x; L_m)\, p(L_m)$$

where the implicit dependencies on both sides have been suppressed. It provides an indication of the relative frequency of overwash for most floes in the floe field described by the FSD. The expected extent $\overline{X}$ is the largest distance x such that

$$\overline{f}_o\left(x; \underbrace{\{d, L_{crit}, L_{\min}, \gamma_1, \gamma_2\}}_{\text{floe field}}, \underbrace{\{H_s, \tau_p\}}_{\text{wave}}\right) > f_{tol}.$$

It is the largest distance that most floes in the floe field are predicted to be overwashed.

4. Comparison With Wave Basin Experiments

A laboratory experiment that investigated interactions between incoming regular and irregular waves and an array of model floes (wooden disks) was conducted in 2013 at the Basin de Génie Océanique FIRST wave basin facility, located at Océanide, La Seyne sur Mer, France. A schematic of the experimental setup is given in Figure 7a with the experimental model parameters provided in Table 1. Across a series of separate tests, the wave maker on the left of the tank generated rightward propagating regular and irregular waves (Table 2), which were transmitted and reflected as they passed through the model floes (brown circles). The array had a concentration of $c_f = 0.39$ and the maximum number of floes in the direction of wave propagation was three. The transmitted waves were dissipated by the beach. Four cameras (red squares) were situated above the floes, allowing them to be observed throughout the experiment. Overwash of the array was observed as a consistent buildup of water on the surface of the floes throughout the experiment.

Given the floe field and incoming wave properties in Tables 1 and 2, we use the model to predict the maximum extent X_L of overwash for a three floe transect in the degenerate case where all floe properties and their respective counts are known. We report the results as the number of floes overwashed along the transect M_X, which is $M_X = c_f X_L / L$. We set the wave dissipation function $\mathcal{T}_{diss}$ to unity as attenuation due to scattering dominates for the wavelength to floe length ratios in the experiment (Bennetts & Williams, 2015; Toffoli et al., 2022). For the regular waves, the values A and τ describe a single incoming wave for which the overwash extent is predicted. For the irregular waves, the values H_s and τ_p describe an ensemble of waves for which the ensemble average overwash extent is predicted. The model predictions and experimental observations agree well for a range of overwash behaviors from no floes overwashed to all floes overwashed (Figure 7).

The regular wave results (Figure 7b) provide insight into the effect of the incoming wave properties on the extent of overwash. As expected, increasing the wave amplitude increases the extent of overwash into a floe field. Increasing the wave period increases the extent at first and then begins to decrease the extent. The period dependence is a result of the relative wavelength (period/frequency) dependence of the floe–wave motions discussed in Section 3.1.2. Larger reflection of energy makes individual floes easier to overwash but also decreases the transmission of wave energy farther into the floe field. When wavelengths are small compared to floe thickness and length (small periods), most energy is reflected and the floe is approximately still. The large reflection and negligible movement of the floe results in the first floe overwashing with the least incoming amplitude (energy), which corresponds to $A \approx d_f/2$. Overwashing subsequent floes requires ever larger incoming amplitudes (energy) as most wave energy is reflected and thus not transmitted. In contrast, when wavelengths are long compared to floe thickness and length (long periods), then most energy is transmitted. The significant transmission of waves causes the first floe to require greater incoming amplitudes (energy) to overwash as wave reflection is reduced, but, once achieved, overwash extends deep into the floe field. The large transmission of wave energy for longer
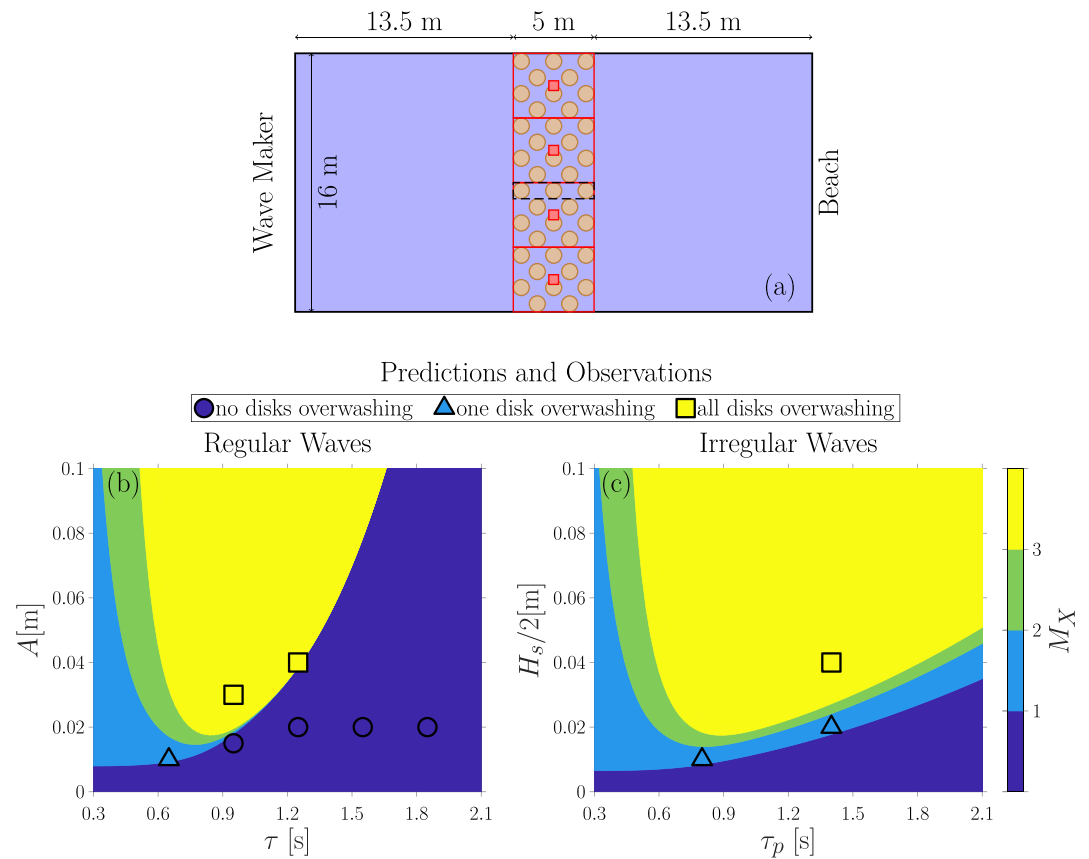
Figure 7. (a) Schematic of the experimental setup showing wooden disks (⬤), camera locations (🟥), camera field of view (▭), and the three floe transect used for observations of overwash (▭). Comparison of model predictions of number of floes overwashed (M_X) with experimental observations for the (b) regular and (c) irregular wave tests. The color bar describes the model result by highlighting the bounds of M_X, so ■ corresponds to no floes overwashing (less than 1), while ■ corresponds to one floe overwashing (above 1 but less than 2).

periods becomes extreme for $\tau > 1$ s, resulting in predictions of either no floes overwashing or all floes overwashing. Due to the competition between reflection and transmission, each overwash extent has a period at which the incoming amplitude that achieves the extent is minimized, and this period and its associated amplitude increase as the overwash extent does.

The irregular wave model predictions of overwash extent (Figure 7c) demonstrate dependencies on $H_s/2$ and τ_p, which are qualitatively similar to the dependencies on A and τ for the regular wave predictions. The behavior for short τ_p is almost identical to short τ regular waves as most of the wave energy lies in frequencies (wavelengths) in the large reflection regime, meaning overwash requires smaller incoming $H_s/2$ but does not penetrate far into the floe field. The similarity between the results for irregular and regular waves extends to the minimum $H_s/2$ and corresponding τ_p (or A and τ) required to produce an overwash extent. As τ_p (or τ) increases, the overwash extent produced by $H_s/2$ (or A) is greater for the irregular waves than the regular waves. This is because all the frequency

Table 1
Comparison of Laboratory Parameters, Their Field Equivalent Under Froude Similitude, and the Values in Section 5

Setting	d [m]	L [m]	ρ'/ρ	E [GPa]	H [m]	A (or $H_s/2$) [m]	τ (or τ_p) [s]
Experiment	0.033	0.99	0.545	4	3.1	0.01–0.04	0.65–1.4
Experiment (Scaled)	3.3	99	0.545	400	310	1–4	6.5–14
Modeled fields (Section 5)	0–10	0–100	0.897	6	1,000	0–7	0–20

Note. The floes had Poisson ratio $\nu = 0.3$.

Table 2
Incoming Waves Properties for the Separate Regular (Amplitude A and Period τ) and Irregular (Significant Wave Height H_s and Peak Period τ_p) Tests

τ or τ_p [s]	0.65	0.95	0.95	1.25	1.25	1.55	1.85	0.8	1.4	1.4
A or $H_s/2$ [m]	0.01	0.015	0.03	0.02	0.04	0.02	0.02	0.01	0.02	0.04

Note. Irregular waves followed the JONSWAP spectrum (Equation 3).

components of the irregular waves contribute to the coupled floe–wave motions, which can drive overwash. Further, the condition on overwash of irregular waves $f_o > f_{tol} = 0.05$ is weaker than in the regular wave case, where either $f_o = 1$ or $f_o = 0$. The presence of multiple wave frequencies for irregular waves produces a gradual transition between all floes overwashing or no floes overwashing for $\tau_p > 1$ s, as opposed to the abrupt transition for regular waves when $\tau > 1$ s (Figure 7b). Both regular and irregular wave overwash extent predictions do not demonstrate effects from resonant responses in the coupled–floe wave motions as M_X contours are smooth and there are no pronounced peaks in M_X for particular τ_p (or τ). The lack of resonant effects for overwash extent is explained by the lack of these effects on individual floe overwash predictions as demonstrated in Figure 5 and also on attenuation due to the floe field as demonstrated in Figure 6.

The model predictions of overwash extent agree well with experimental observations, justifying the classification of overwash behavior using the chosen tolerance of overwash frequency $f_{tol} = 0.05$ for single and multiple floes. The occurrence of overwash increases attenuation of wave energy (Bennetts & Williams, 2015; Toffoli et al., 2022), which is not accounted for in the model. Despite this, the agreement between predictions and observations of overwash extent is maintained. As the experiment did not measure the depth or frequency of overwash, the accuracy of the computed f_o and associated overwash depths cannot be verified. Laboratory experiments using a single model floe under regular wave action (Skene et al., 2015) demonstrate that equivalent predictions of f_o and associated overwash depths are accurate, justifying their use in the overwash model.

Table 1 also provides the experiment scaled using 1:100 Froude similarity and the range of values used to model sea ice floes in Section 5. The wave conditions in the experiment are in good agreement with their field equivalents studied in Section 5. However, the scaled floes correspond to much larger floes at field scales than those in Section 5, where the average ice thickness is 0.5–1 m and the average floe length is 0.7–5 m. Additionally, the scaled floes are significantly less dense and more rigid than sea ice. The model predicts greater overwash for the scaled floes than most floes investigated in Section 5. The decrease in overwash produced by a lower density and larger thickness being overcome by an increase in overwash due to increased rigidity (Tran-Duc et al., 2020) and length. The underlying model of coupled floe–wave motions has been validated for a variety of geometries, densities, and Young's moduli (Bennetts et al., 2015; Meylan, Bennetts, et al., 2015; Toffoli et al., 2015), including those better resembling sea ice, giving confidence to its use in the overwash extent model and thus the predictions in Section 5. Finally, the comparison to the experiment does not validate the modeled attenuation due to dissipation, which is important for long waves in the MIZ and remains a major challenge for MIZ models (Squire, 2020).

5. Predictions of Overwash Extent in the MIZ

We investigate the extent of overwash for fragmented (Toyota et al., 2011) and pancake (Alberello et al., 2019) floe fields described in Section 3.2.1. We model fields of ice floes with uniform density, Young's modulus, and Poisson ratio, which have a constant typical thickness (d) and lengths (L) that vary randomly according to a prescribed FSD. The floe fields have a compact ice edge after which the FSD and floe concentration ($c_f = 0.6$) are constant. We model incoming ocean swell using the JONSWAP spectra (Equation 3) with various values of H_s and τ_p prescribed. We then produce the predicted extent of overwash for a section of the Antarctic MIZ using the floe field and incoming wave properties around the South African icebreaker S.A. Agulhas II on a July 2017 voyage, during which the wave evolution and the FSD in the MIZ were monitored by an onboard stereo-camera system (Alberello et al., 2019, 2022). The MIZ observed by the S.A. Agulhas II had a diffuse ice edge, which we accounted for in the predictions using satellite-derived ice concentrations.
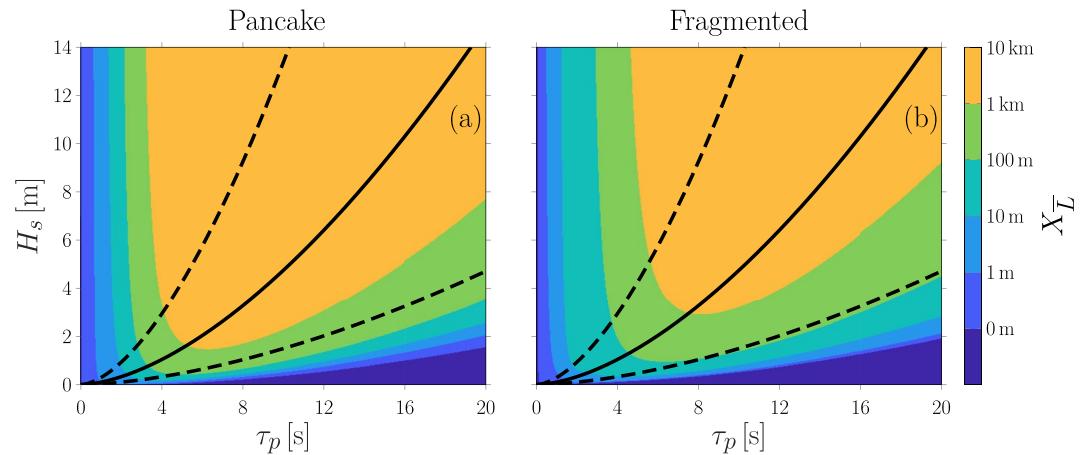
Figure 8. Dependence of maximum overwash extent on incoming wave spectra for a floe with mean length in (a) pancake $\left(L = \overline{L} = 0.7\,\text{m}\right)$ and (b) fragmented $\left(L = \overline{L} = 5\,\text{m}\right)$ floe fields. Overlaid are the typical (—), maximum (— —), and minimum (— —) H_s-τ_p relationships (Equation 15) for the available wave data in the Southern Ocean (Young et al., 2020).

5.1. Overwash Extent for Floe With Given Properties

5.1.1. Effect of Incoming Wave Spectra

Figure 8 shows the dependence of X_L on the incoming H_s- and τ_p-values, for the floe of mean length in (a) pancake and (b) fragmented floe fields. For both floe fields, increasing H_s increases overwash extent and increasing τ_p at first increases overwash extent and then decreases overwash extent past some critical peak periods. The relationships match those found in the experimental validation (Figure 7c), indicating that these relationships hold despite the inclusion of wave dissipation and the random variation of floe lengths according to the FSD.

In the Southern Ocean, mean values of H_s are between 3 and 6 m (Young et al., 2020) with measured values up to $H_s = 14$ m (Young et al., 2020). Peak periods and significant wave heights tend to exhibit the following relationship (Young et al., 2020)

$$H_s = 4\sqrt{cu_{10}^{0.7}g^{1.3}\tau_p^{3.3}}, \tag{15}$$

where u_{10} is the wind speed 10 m above the ocean surface and c is a data fitting constant. We fix u_{10} to its annual mean value of 12 m s^{-1} (Young et al., 2020). The line of best fit gives the typical H_s-τ_p relationship with $c = 6.36531026 \times 10^{-6}$. Additional H_s-τ_p relationships that maintain the fundamental shape can be constructed by changing c. For the available wave data in the Southern Ocean (Young et al., 2020), we produced a maximum (all wave data lay below) and a minimum (all wave data lay above) H_s-τ_p relationship using $c = 5.0559 \times 10^{-5}$ and $c = 6.3650 \times 10^{-7}$, respectively.

Considering only the H_s- and τ_p-values between the maximum and minimum relationships (dashed lines) provides predictions of typical overwash extents for the mean floe in pancake and fragmented floe fields. For the pancake floe field (Figure 8a), the maximum overwash extent for the mean floe length in mean seas ($H_s = 3$–6 m) is in the range 100 m–10 km. For mean seas, extents are typically over 1 km with the exception being those with comparatively long τ_p as indicated by Equation 15 (closer to bottom dashed line). Maximum extents are also less than 1 km for calm seas with $H_s \leq 2$ m. For the fragmented floe field in mean seas, typically $100\,\text{m} < X_{\overline{L}} < 10\,\text{km}$. Overwash extents over 1 km occur for mean seas with corresponding τ_p approximately given by Equation 15, whereas overwash extents below 1 km occur for seas with $H_s < 3$ m and those with spectra around the lower bound relationship (bottom dashed line) between H_s and τ_p. Both fragmented and pancake floe fields have $X_{\overline{L}} < 10\,\text{km}$ for even the most energetic seas.

Comparing the predictions of both types of floe field, overwash penetrates less into fragmented floe fields, requiring about twice the H_s values to generate $X_{\overline{L}} \geq 1$ km. The reduction of overwash extents in fragmented floe fields compared to pancake floe fields is due to the floes being longer and thicker. Fields of thicker and longer
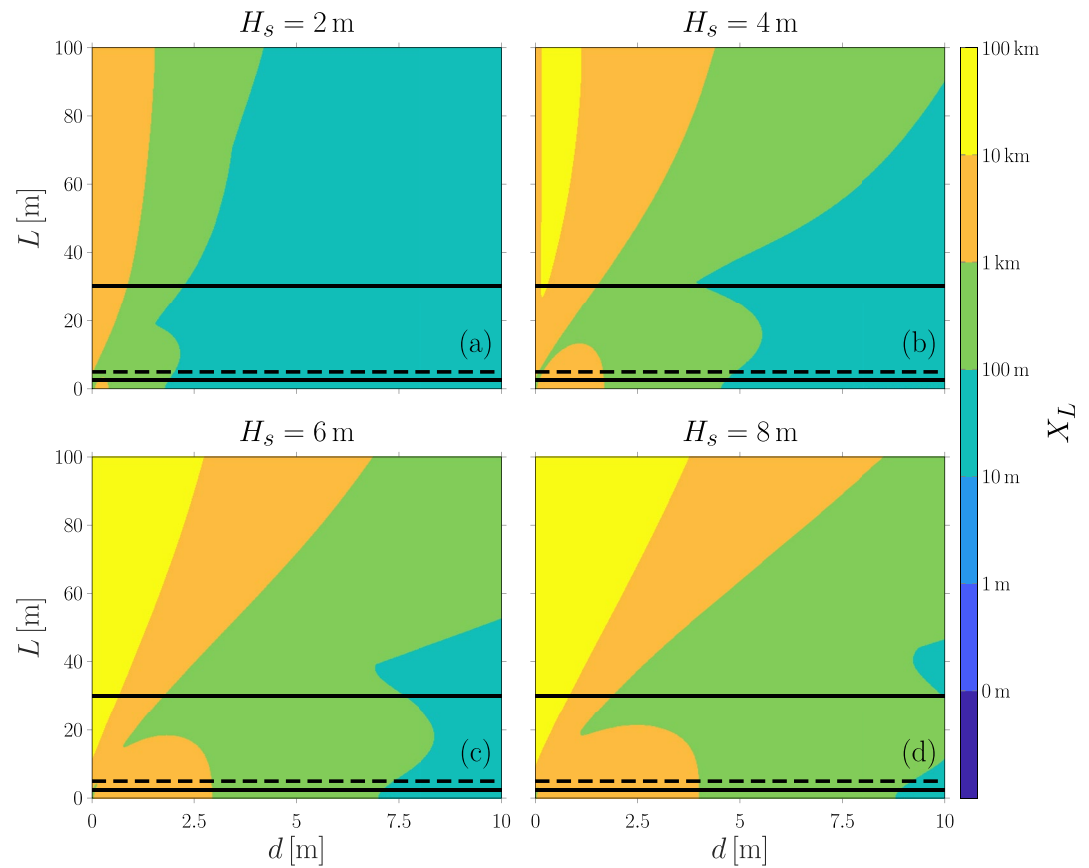
Figure 9. Effect of a particular floe's length L on the maximum overwash extent for a fragmented floe field (Toyota et al., 2011) with uniform thickness d and $c_f = 0.6$ for a variety of incoming ocean waves. The FSD parameters of L_{crit} and L_{min} (━) as well as $\overline{L}$ (━ ━) are demonstrated. The various incoming ocean wave spectra have the provided H_s-values with τ_p-values determined from Equation 15.

floes reflect more wave energy decreasing the extent of overwash. Thicker floes also have larger freeboards making them more difficult to overwash.

5.1.2. Effect of Floe Properties

Figure 9 shows the dependence of the maximum overwash extent for a floe in a fragmented floe field on the floe's length and the uniform thickness of the floe field. Results are shown for four different H_s-values with the corresponding τ_p-value for each H_s-value determined by Equation 15. Changes in floe length affect the chosen floe only with the lengths of all other floes in the floe field determined by the FSD. The mean floe size, $\overline{L}$, is indicated on the plots, along with L_{min} and L_{crit}, with 97% of floes having lengths between these values. In contrast, we assumed a constant floe thickness for the floe field for simplicity. Thickness values of order 1 m are expected in a fragmented floe field (Toyota et al., 2011), and so a thickness of 10 m was used as an upper bound.

Figures 9a–9d shows similar qualitative relationships between maximum overwash extent and floe length and thickness. Increasing floe thickness decreases the overwash extent as increasing thickness increases freeboard and wave attenuation, making overwash of individual floes more difficult and reducing overwash extent. Increasing floe lengths increases the maximum overwash extent. Longer floes can be overwashed by longer waves (lower frequency) due to increased wave reflection. Longer waves (lower frequency) travel further into the floe field since the long floes that scatter them are rare in the split power law FSD and so longer floes have larger overwash extents. When the floe lengths and thicknesses are small and of comparable size, there are regions of 100 m and 1 km overwash extent that expand with increasing H_s. These growing regions are a result of a small but consistent amount of overwash of thin floes (with small freeboards) due to the presence of multiple low-frequency (large wavelength) components. Individually, such low-frequency components would not overwash the floe, but
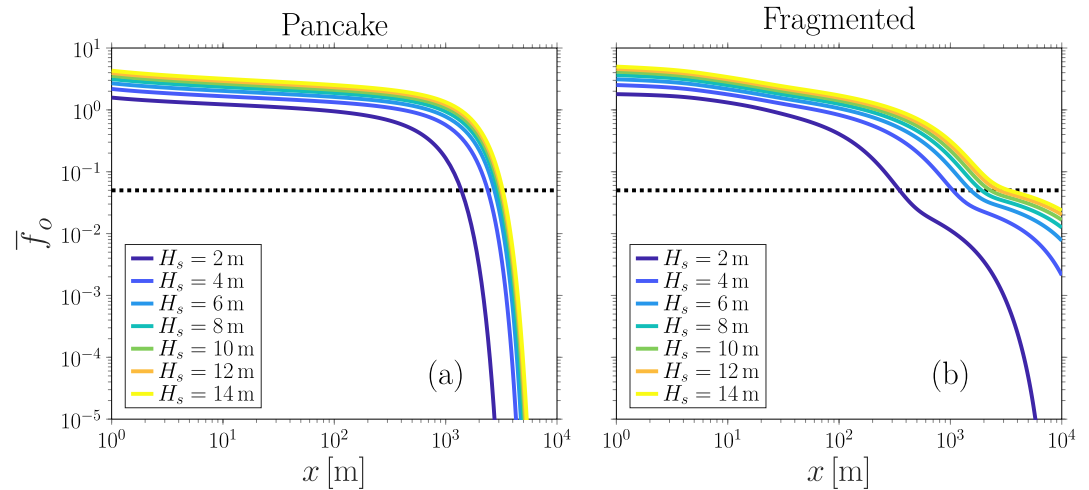
Figure 10. Expected overwash event frequency over distance $\left(\overline{f}_o(x)\right)$ for (a) pancake and (b) fragmented floe fields and various H_s-values where the τ_p-values are given by Equation 15. The tolerance frequency f_{tol} (▬ ▬) is used to determine the expected extent $\overline{X}$.

together they do, and since these are low frequency (large wavelength) waves, they propagate far into the floe field. The contour is growing as incoming H_s increases as the energy in these frequency components grows.

In calm seas ($H_s = 2$ m; Figure 9a), most floes ($L_{\min} < L < L_{crit}$) with $d \leq 1$ m will be overwashed in the range 0.1–1 km into the MIZ. For very thick floe fields with $d \geq 5$ m, almost all floes are only overwashed in at least the first 10 m. For mean to energetic seas (Figures 9b–9d) impacting floe fields with $d \leq 1$ m, extents of 1 km occur for relatively long floes $\left(\overline{L} < L < L_{crit}\right)$. Extents of 10 km are also possible for more energetic seas (Figures 9c and 9d) and long floes ($L > 20$ m) in thin floe fields ($d < 0.5$ m). Extents for floe fields with $d \geq 5$ m typically remain less than 100 m with the exception of relatively long floes $\left(\overline{L} < L < L_{crit}\right)$ for which extents over 100 m are possible. The maximum overwash extent for relatively and extremely long floes $\left(L > \overline{L}\right)$ is most sensitive to increasing H_s, as increasing H_s also increases τ_p, meaning more wave energy at longer periods (wavelengths), which drives the overwash of these long and rare floes. For short $\left(L < \overline{L}\right)$ and thick ($d > 2.5$ m) floes, increasing H_s does not noticeably increase the overwash extent.

5.2. Expected Overwash Frequency in a Floe Field

Figure 10 shows the expected overwash event frequency $\left(\overline{f}_o\right)$ versus distance, for (a) a pancake, and (b) a fragmented floe field, for a range of incoming wave spectra (Equation 3) with various H_s-values where τ_p is given by Equation 15. The value of $f_{tol} = 0.05$ is highlighted to demonstrate the expected overwash extent $\left(\overline{X}\right)$ for each incoming spectrum.

Figures 10a and 10b demonstrates a similar behavior of $\overline{f}_o$ over distance. In particular, $\overline{f}_o$ decreases with increasing distance due to attenuation of the waves driving overwash. The apparent decrease is gradual at first and then takes place rapidly after a kilometer. The gradual and then rapid reduction in $\overline{f}_o$ is caused by the exponential attenuation of the wavefield and enhanced by the logarithmic scale of the plots. Increasing H_s increases $\overline{f}_o$ as expected.

The pancake floe field in calm seas ($H_s = 2$ m; red line) is predicted to have most floes experiencing an overwash event about once every mean period $\left(\overline{f}_o \approx 1\right)$ up to a distance of $x = 100$ m. As distance increases, $\overline{f}_o$ decreases due to attenuation removing wave energy from the frequencies that drive overwash of most floes. After a kilometer, the decrease becomes rapid, and the overwash frequency drops by several orders of magnitude. The overwash frequency drops below $f_{tol} = 0.05$ when $x = \overline{X} = 1.9$ km resulting in an attenuated $H_s = 0.79$ m.
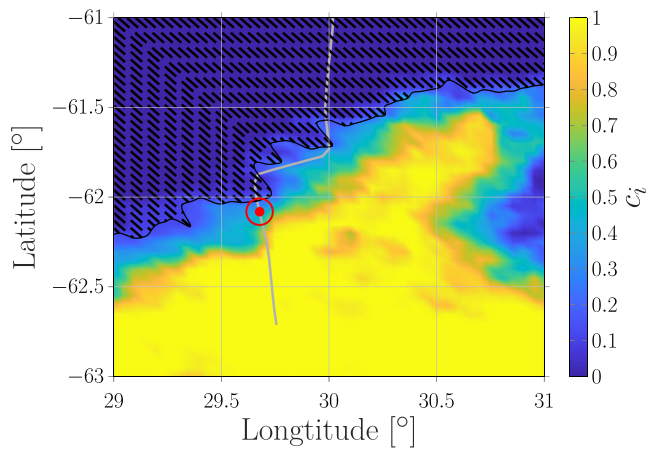
Figure 11. Ice concentration c_i from AMSR2 satellite data (Melsheimer & Spreen, 2019), portion of transects where most floes can be overwashed (▬ ▬), boundary of region most floes can be overwashed (▬) and the path of the S.A. Agulhas II (▬) and the reported location of first measurement (●). The distance traveled during the first wave measurements (○), which took place between 08:00 and 08:30 UTC on the 4 July 2017.

The overwash frequency $\overline{f}_o$ (and thus $\overline{X}$) increases with increasing H_s, but maintains the same qualitative behavior. The increase is greatest when H_s increases from 2 to 4 m ($\overline{X} = 3.6\,$km where $H_s = 2.3\,$m), but has less effect as H_s increases further, for example, by doubling again to $H_s = 8\,$m ($\overline{X} = 3.9\,$km where $H_s = 6.2\,$m). The reduced effect of doubling H_s is due to the exponential nature of attenuation and the associated increase in τ_p (Equation 15). The increase in τ_p removes energy from the short-period (high-frequency) waves that drive overwash as demonstrated by the prediction of no overwash when attenuated H_s values are large. Therefore, in calm seas, most floes in the pancake floe field will overwash at a distance of 1.9 km with more energetic seas ($H_s > 4\,$m) allowing overwash up to distances over 3 km.

The average overwash extent of fragmented floe fields is more sensitive to H_s with calm seas ($H_s = 2\,$m) resulting in $\overline{X} = 400\,$m (attenuated $H_s = 0.8\,$m), and extremely energetic seas ($H_s = 14\,$m) resulting in $\overline{X} = 3.7\,$km (attenuated $H_s = 12\,$m). This greater sensitivity of the fragmented floe field is due to the greater variability in the floe lengths in its FSD. Of particular importance is the larger presence of longer floes in the fragmented floe field for which overwash is more likely. The shape of $\overline{f}_o$ over distance is different for fragmented floe fields (although the overall trends are the same), in particular, the second region of gradual decrease in $\overline{f}_o$ around the value of f_{tol}. This shape difference is due to the increased role of scattering on attenuation for the fragmented floe field as more floes have lengths and thickness comparable to the wavelengths investigated.

5.3. Overwash Extents Versus Field Observation Locations

On 4 July 2017, the South African icebreaker S.A. Agulhas II entered the Antarctic MIZ with a polar cyclone nearby (Alberello et al., 2019, 2022; Vichi et al., 2019). An onboard stereo-camera system was used to monitor waves and floe sizes in the MIZ over 30 min intervals at six locations as the S.A. Agulhas II progressed deeper into the MIZ up to 40 km from the ice edge. Analysis of the floe sizes by Alberello et al. (2019) produced the pancake floe field FSD described in Section 3.2.1. Maximum wave heights greater than 9 m were recorded over 20 km into the MIZ (Alberello et al., 2022). Figure 11 shows the average ice concentration c_i during the day of the voyage from the AMSR2 satellite data (Melsheimer & Spreen, 2019) and the incoming track of the S.A. Agulhas II, which begins at $-61°$ latitude and continues down to $-62.7°$. The first series of stereo-camera images were acquired between 08:00 and 08:30 UTC (red circle).

Model predictions of expected overwash extent $\left(\overline{X}\right)$ along transects in the mean wave direction are overlaid, and these transects are combined to produce a prediction of the region in which most floes in the floe field will be overwashed. The incoming wave spectra for the transects are the JONSWAP spectrum (Equation 3) where H_s- and τ_p-values are given by the ECMWF ERA5 wave reanalysis (Hersbach et al., 2020) at 08:00 UTC at the 61st parallel south. The floe concentration, c_f, was measured along the ship track in the MIZ (Alberello et al., 2019); however, the limited spatial extent makes this c_f insufficient when modeling the region depicted in Figure 11. Therefore, the ice concentration c_i derived from AMSR2 satellite data (Melsheimer & Spreen, 2019), which combines floe and interstitial ice concentrations, is used as an estimate for the floe concentration c_f.

The predictions of expected overwash extent demonstrate that the first analysis of stereo-camera images commenced very close to the location at which overwash becomes unlikely to occur, and hence, all subsequent images are beyond the overwash region. Overwash remains restricted to the outermost region of the MIZ (taken to be where $c_i > 0.01$) with a farthest penetration of 16 km where the ice concentration remained low over significant distances between 29° and 29.5° east longitude. The highest ice concentration where overwash is predicted to occur is $c_i \approx 0.4$, which occurred only 7 km into the MIZ at around 61.5° south latitude. Inside the predicted region of overwash, the model indicates that most floes will overwash at least once every 20 mean periods $\left(\overline{f}_o > 0.05\right)$. In the overwash region, $\overline{f}_o$ has a mean value 1.3 and so most floes have an overwash event about once every 1.3 times the mean period. The mean is much higher than f_{tol} as that is the cutoff and because $\overline{f}_o$

reduces quite rapidly over long distances as shown in Figure 10. Using the peak period measured during the voyage to approximate the mean period, that is, $\overline{\tau}_I(0) \approx \tau_p = 12$ s (Alberello et al., 2022), an observer on a ship should expect to see overwash events about once every 16 s and at least once every 4 min.

6. Conclusions and Discussion

We have developed a novel model of the extent of wave overwash in the MIZ that incorporates the stochastic nature of the irregular incoming waves and floe sizes. The model produces the expected frequency of overwash events, given the underlying FSD, indicating the frequency of overwash events for most floes in the MIZ. Most floes are said to be overwashing when the expected frequency of overwash events is greater than 0.05, so that an overwash event occurs at least once every 20 mean wave periods. Model predictions were given for floe fields with a compact ice edge and a uniform concentration thereafter. We investigated pancake floe fields, based on measurements from the Antarctic MIZ during the winter ice advance (Alberello et al., 2019), and fragmented floe fields, based on measurements from the Weddell Sea at the beginning of the spring ice retreat (Toyota et al., 2011). For typical sea states, with significant wave heights 2–6 m and associated peak periods, most floes were overwashed 1.9–3.9 km into the pancake floe field, at which point H_s had attenuated to 0.8–4.2 m. For a fragmented floe field in the same seas, most floes were overwashed up to 0.4–3.1 km, at which point H_s had attenuated to 0.8–4.2 m. These predictions provide only the average overwash behavior for the ensemble of possible floe fields and incoming waves. For example, floes that are exceptionally long for the FSD may be overwashed far deeper into the MIZ as in Figure 9 and very large individual waves, for instance, a 26.4 m wave recorded in the open Southern Ocean (Young et al., 2020) may generate overwash far deeper into the MIZ. The limited extent of predicted average overwash into both types of floe fields and the need for relatively large waves needed to produce overwash extents over 3 km help to explain the scarcity of in situ reports of overwash in the MIZ.

The overwash extent was larger for the pancake floe field than the fragmented floe field as pancake floes were smaller and thinner. All else being equal (i.e., incoming waves and ice concentrations), this indicates that overwash extents are greater during autumn–winter (when ice is advancing and the MIZ is dominated by pancake floes) than spring–summer (when ice is retreating and the MIZ is dominated by fragmented floes). Further, waves in the Southern Ocean are typically most energetic in winter (Young et al., 2020), which will produce greater overwash extents. Seasonal changes in ice conditions, such as floe sizes (Nihashi & Ohshima, 2001) and ice concentrations (Cavalieri & Parkinson, 2008), are likely a factor as they tend to increase in autumn–winter (reducing overwash extent) and decrease in spring–summer (increasing overwash extent).

The overwash extent was predicted for incoming waves and a floe field representative of the conditions during an experiment in the winter Antarctic MIZ that coincided with a polar cyclone. The experiment used a stereo-camera system (Alberello et al., 2019, 2022), which could have, in principle, captured overwash events but did not. Our model predicts that, in these conditions, overwash is limited to the outskirts of the MIZ where ice concentrations are <0.4 and before the first analyzed images were acquired. Therefore, the predictions suggest that prospective field studies targeting overwash, using a stereo-camera system or equivalent, will need to take place closer to the open ocean. In this case, the model predictions from Section 5.2 indicate that measurements could be taken during mean sea-state conditions (i.e., not during a cyclone) as overwash would still persist over several kilometers from the ice edge. The significantly larger distances over which most floes were predicted to overwash, compared to the studied fixed concentration floe fields, demonstrate the significant role lower ice concentrations play in increasing overwash extent. Thus, banded and diffuse ice edges (see Figure 1 in Massom & Stammerjohn, 2010) will experience larger overwash extents than compact ice edges.

Predicting coupled floe–wave motions is a core component of our overwash model. They are modeled using an elastic plate, neglecting certain physical processes, such as drift, collisions, rafting, viscosity in the floe response, and overwash loading. Floe drift, which moves the floe relative to the wavefield, decreases overwash depths (Nelli et al., 2017; Tavakoli & Babanin, 2021). Collisions between floes generate overwash (Toffoli et al., 2022) and move the floes relative to the wavefield. Floe rafting increases the apparent length of a floe, which the model predicts will allow floes to overwash more readily. The presence of overwash suppresses the motions of the floe (Nelli et al., 2020) impacting whether the floe will overwash as subsequent waves pass. Currently, collisions, rafting, drift, and overwash can be simulated using computational fluid dynamics software (Huang et al., 2020; Nelli et al., 2020; Tavakoli & Babanin, 2021) or modeled assuming a known decoupled wavefield (Herman et al., 2019; Shen et al., 2001; Skene & Bennetts, 2021) with the former being prohibitively expensive for large-scale modeling

and the latter currently unable to provide insight into the coupled effects on overwash. Numerical simulations would be a useful benchmark for the coupled floe–wave motion model component, avoiding the challenges of laboratory and field experiments and allowing the influence of these effects to be tested and compared. Viscosity in the response of ice floes to passing waves (Timco & Weeks, 2010) will alter its overwash behavior with floes that conform well to the sea surface generating less overwash (Tran-Duc et al., 2020). The elastic floe assumption could be relaxed by using viscoelastic floe models (Sree et al., 2020).

Our model assumes that incoming waves (incoming spectrum), floe field conditions (FSD and ice concentration), and ice properties (density and Young's modulus) are steady. Since the criterion defining overwash ensures that at least one overwash event occurs every 20 mean periods, this is the natural time scale over which the incoming waves, floe field conditions, and ice properties should be constant for the model to be valid. Since mean periods in the MIZ are of the order of tens of seconds (Alberello et al., 2022; Meylan et al., 2014), the assumption that waves, floe field conditions, and ice properties do not change over the order of minutes to tens of minutes is reasonable. Additionally, the developed overwash extent model could be adapted to allow the modeling of time-dependent effects that occur over much longer time scales than minutes to tens of minutes, such as the impact of overwash on growth (Doble, 2003) and melt (Massom et al., 2001) of floes. In contrast, the overwash extent model is not suitable for much shorter time scales, such as the transient waves generated by a passing ship (e.g., Dumas-Lefebvre & Dumont, 2021).

In conclusion, we have developed a model that predicts the extent of wave overwash of ice floes in the MIZ for specified incoming waves and floe fields. Model outputs, for the degenerate case where the floe thicknesses and lengths are known, were validated using the only available data from a laboratory wave basin experiment involving an array of artificial floes. Overwash is a critical component to the evolution of the MIZ as it dissipates wave energy, can remove snow from the surface of floes (Massom et al., 1998), and deposits water on a floe's surface. The resultant water on a floe's surface is likely to enhance both growth (Doble, 2003) and melt (Massom et al., 2001) of floes and hosts biota (Ackley & Sullivan, 1994). Overwash and its resultant attenuation and thermodynamic and biogeochemical effects are currently absent from models of sea ice. Our proposed overwash extent model can be integrated within current sea ice models (e.g., Hunke et al., 2010), provides a basis for an overwash dissipation model for floe fields, and can be used to guide future field observations of overwash.

Appendix A: Overwash Simulation

Given an incoming spectrum S, a realization of the incoming waves from Equation 1 that is a sample of the random phases θ_n (uniform-distributed) and the random amplitudes A_n (Rayleigh-distributed with mean $\sqrt{2S(\omega_n)\Delta\omega}$) is produced. For each regular wave component of this incoming realization, the propagating solutions of Bennetts et al. (2007) produce the reflection ($R(\omega)$) and transmission ($T(\omega)$) coefficients as well as the plate movement coefficients for each location $x\left(\hat{\zeta}(x,\omega)\right)$. From these coefficients, the left and right wavefields as well as the plate movements are given by

$$\eta_l(x,t) = \sum_{n=1}^{N} A_n \operatorname{Re}\left\{\left(1 + R(\omega_n)e^{-2ik_nx}\right)e^{i(k_nx-\omega_nt+\theta_n)}\right\},$$

$$\eta_r(x,t) = \sum_{n=1}^{N} A_n \operatorname{Re}\left\{T(\omega_n)e^{i(k_nx-\omega_nt+\theta_n)}\right\},$$

$$\zeta(x,t) = \sum_{n=1}^{N} A_n \operatorname{Re}\left\{\hat{\zeta}(x,\omega_n)e^{i(k_nx-\omega_nt+\theta_n)}\right\}.$$

The velocity at the free surface can also be obtained from these and is given by

$$u_l(x,0,t) = \sum_{n=1}^{N} A_n \frac{gk_n}{\omega_n} \operatorname{Re}\left\{\left(1 + R(\omega_n)e^{-2ik_nx}\right)e^{i(k_nx-\omega_nt+\theta_n)}\right\} \quad \text{and}$$

$$u_r(x,0,t) = \sum_{n=1}^{N} A_n \frac{gk_n}{\omega_n} \operatorname{Re}\left\{T(\omega_n)e^{i(k_nx-\omega_nt+\theta_n)}\right\}.$$

Realizations of the sea surface coupled with the nonlinear shallow water equations (SWEs) for a horizontal bed are used to simulate overwash on the floe surface as performed by Skene et al. (2015). The nonlinear SWEs for a horizontal bed are

$$\frac{\partial h}{\partial t} + \frac{\partial (uh)}{\partial x} = 0,$$

$$\frac{\partial (uh)}{\partial t} + \frac{\partial}{\partial x}\left(u^2 h + \frac{gh^2}{2}\right) = 0,$$

for $x \in [0, d]$, where $h(x, t)$ is the overwash depth, $u(x, t)$ is its depth-averaged horizontal velocity. Homogeneous initial conditions are applied, that is, $h(x, 0) = 0$ and $u(x, 0) = 0$, and overwash is forced by the boundary conditions

$$h(0, t) = \eta_l(0, t), \quad h(d, t) = \eta_r(d, t), \quad u(0, t) = u_l(x, 0, t) \quad \text{and} \quad u(d, t) = u_r(x, d, t).$$

The initial–boundary-value problem is solved using the numerical method described by Skene et al. (2015), producing the simulation of overwash.

Data Availability Statement

The code to run the overwash extent model can be downloaded at https://doi.org/10.5281/zenodo.7073225. The coefficient values from the coupled floe–wave motion sub-model (required by the extent model) and the data required to produce Figure 11 can be downloaded at https://doi.org/10.5281/zenodo.7059554.

References

Ackley, S. F., & Sullivan, C. W. (1994). Physical controls on the development and characteristics of Antarctic sea ice biological communities–a review and synthesis. *Deep Sea Research Part I: Oceanographic Research Papers*, *41*(10), 1583–1604. https://doi.org/10.1016/0967-0637(94)90062-0

Alberello, A., Bennetts, L. G., Onorato, M., Vichi, M., MacHutchon, K., Eayrs, C., et al. (2022). Three-dimensional imaging of waves and floes in the marginal ice zone during a cyclone. *Nature Communications*, *13*(1), 4590. https://doi.org/10.1038/s41467-022-32036-2

Alberello, A., Dolatshah, A., Bennetts, L. G., Onorato, M., Nelli, F., & Toffoli, A. (2021). A physical model of wave attenuation in pancake ice. *International Journal of Offshore and Polar Engineering*, *31*(3), 263–269. https://doi.org/10.17736/ijope.2021.ik08

Alberello, A., Onorato, M., Bennetts, L. G., Vichi, M., Eayrs, C., MacHutchon, K., & Toffoli, A. (2019). Brief communication: Pancake ice floe size distribution during the winter expansion of the Antarctic marginal ice zone. *The Cryosphere*, *13*(1), 41–48. https://doi.org/10.5194/tc-13-41-2019

Ardhuin, F., Sutherland, P., Doble, M., & Wadhams, P. (2016). Ocean waves across the Arctic: Attenuation due to dissipation dominates over scattering for periods longer than 19s. *Geophysical Research Letters*, *43*(11), 5775–5783. https://doi.org/10.1002/2016GL068204

Armstrong, T., & Roberts, B. (1956). Illustrated ice glossary. *Polar Record*, *8*(52), 4–12. https://doi.org/10.1017/S0032247400045599

Bai, W., Zhang, T., & McGovern, D. J. (2017). Response of small sea ice floes in regular waves: A comparison of numerical and experimental results. *Ocean Engineering*, *129*(November 2016), 495–506. https://doi.org/10.1016/j.oceaneng.2016.10.045

Bennetts, L. G., Alberello, A., Meylan, M. H., Cavaliere, C., Babanin, A. V., & Toffoli, A. (2015). An idealised experimental model of ocean surface wave transmission by an ice floe. *Ocean Modelling*, *96*, 85–92. https://doi.org/10.1016/j.ocemod.2015.03.001

Bennetts, L. G., Biggs, N. R., & Porter, D. (2007). A multi-mode approximation to wave scattering by ice sheets of varying thickness. *Journal of Fluid Mechanics*, *579*, 413–443. https://doi.org/10.1017/S002211200700537X

Bennetts, L. G., O'Farrell, S., & Uotila, P. (2017). Brief communication: Impacts of ocean-wave-induced breakup of Antarctic sea ice via thermodynamics in a stand-alone version of the CICE sea-ice model. *The Cryosphere*, *11*(3), 1035–1040. https://doi.org/10.5194/tc-11-1035-2017

Bennetts, L. G., & Squire, V. A. (2012a). Model sensitivity analysis of scattering-induced attenuation of ice-coupled waves. *Ocean Modelling*, *45–46*, 1–13. https://doi.org/10.1016/j.ocemod.2012.01.002

Bennetts, L. G., & Squire, V. A. (2012b). On the calculation of an attenuation coefficient for transects of ice-covered ocean. *Proceedings of the Royal Society A: Mathematical, Physical & Engineering Sciences*, *468*(2137), 136–162. https://doi.org/10.1098/rspa.2011.0155

Bennetts, L. G., & Williams, T. D. (2015). Water wave transmission by an array of floating discs. *Proceedings of the Royal Society A: Mathematical, Physical & Engineering Sciences*, *471*. https://doi.org/10.1098/rspa.2014.0698

Cavalieri, D. J., & Parkinson, C. L. (2008). Antarctic sea ice variability and trends, 1979–2006. *Journal of Geophysical Research*, *113*(C7), 1–19. https://doi.org/10.1029/2007jc004564

Cheng, S., Tsarau, A., Evers, K. U., & Shen, H. (2019). Floe size effect on gravity wave propagation through ice covers. *Journal of Geophysical Research: Oceans*, *124*(1), 320–334. https://doi.org/10.1029/2018JC014094

Collins, C. O., Rogers, W. E., Marchenko, A., & Babanin, A. V. (2015). In situ measurements of an energetic wave event in the Arctic marginal ice zone. *Geophysical Research Letters*, *42*(6), 1863–1870. https://doi.org/10.1002/2015GL063063

Doble, M. J. (2003). Pancake ice formation in the Weddell Sea. *Journal of Geophysical Research*, *108*(C7), 3209. https://doi.org/10.1029/2002jc001373

Dolatshah, A., Nelli, F., Bennetts, L. G., Alberello, A., Meylan, M. H., Monty, J. P., & Toffoli, A. (2018). Hydroelastic interactions between water waves and floating freshwater ice. *Physics of Fluids*, *30*(9), 091702. https://doi.org/10.1063/1.5050262

Dumas-Lefebvre, E., & Dumont, D. (2021). Aerial observations of sea ice break-up by ship waves. *The Cryosphere Discussions*, *2021*, 1–26. https://doi.org/10.5194/tc-2021-328

Finocchio, P. M., Doyle, J. D., Stern, D. P., & Fearon, M. G. (2020). Short-term impacts of Arctic summer cyclones on sea ice extent in the marginal ice zone. *Geophysical Research Letters*, *47*(13). https://doi.org/10.1029/2020GL088338

Frankenstein, S., Loset, S., & Shen, H. H. (2001). Wave-ice interactions in Barents Sea marginal ice zone. *Journal of Cold Regions Engineering*, *15*(2), 91–102. https://doi.org/10.1061/(asce)0887-381x(200115:2(91)

Hasselmann, K., Barnett, T. P., Bouws, E., Carlson, H., Cartwright, D. E., Enke, K., et al. (1973). Measurements of wind-wave growth and swell decay during the Joint North Sea Wave Project (JONSWAP). *Deutsche Hydrographische Zeitschrift*, *A8*(12), 95.

Herman, A., Cheng, S., & Shen, H. H. (2019). Wave energy attenuation in fields of colliding ice floes – Part 1: Discrete-element modelling of dissipation due to ice–water drag. *The Cryosphere*, *13*(11), 2887–2900. https://doi.org/10.5194/tc-13-2887-2019

Hersbach, H., Bell, B., Berrisford, P., Hirahara, S., Horányi, A., Muñoz-Sabater, J., et al. (2020). The ERA5 global reanalysis. *Quarterly Journal of the Royal Meteorological Society*, *146*(730), 1999–2049. https://doi.org/10.1002/qj.3803

Holthuijsen, L. H. (2010). *Waves in oceanic and coastal waters*. Cambridge University Press. https://doi.org/10.1017/CBO9780511618536

Huang, L., Lu, W., Yang, J., & Dong, Q. (2022). Experimental study on surface waves around a novel model of ice floe. *Cold Regions Science and Technology*, *193*(August 2021), 103380. https://doi.org/10.1016/j.coldregions.2021.103380

Huang, L., Ren, K., Li, M., Tuković, Ž., Cardiff, P., & Thomas, G. (2019). Fluid-structure interaction of a large ice sheet in waves. *Ocean Engineering*, *182*(May), 102–111. https://doi.org/10.1016/j.oceaneng.2019.04.015

Huang, L., & Thomas, G. (2019). Simulation of wave interaction with a circular ice floe. *Journal of Offshore Mechanics and Arctic Engineering*, *141*(4). https://doi.org/10.1115/1.4042096

Huang, L., Tuhkuri, J., Igrec, B., Li, M., Stagonas, D., Toffoli, A., et al. (2020). Ship resistance when operating in floating ice floes: A combined CFD&DEM approach. *Marine Structures*, *74*, 102817. https://doi.org/10.1016/j.marstruc.2020.102817

Hunke, E. C., Lipscomb, W. H., Turner, A. K., Jeffery, N., & Elliott, S. (2010). *CICE: The los Alamos sea ice model documentation and software user's manual version 4.1 LA-CC-06-012* (Vol. 675, p. 500). T-3 Fluid Dynamics Group, Los Alamos National Laboratory.

Hwang, B., Wilkinson, J., Maksym, T., Graber, H. C., Schweiger, A., Horvat, C., et al. (2017). Winter-to-summer transition of Arctic sea ice breakup and floe size distribution in the Beaufort Sea. *Elementa*, *5*. https://doi.org/10.1525/elementa.232

Kohout, A. L., Williams, M. J., Toyota, T., Lieser, J., & Hutchings, J. (2016). In situ observations of wave-induced sea ice breakup. *Deep-Sea Research Part II Topical Studies in Oceanography*, *131*, 22–27. https://doi.org/10.1016/j.dsr2.2015.06.010

Lever, J., Attwood, D., & Sen, D. (1988). Factors affecting the prediction of wave-induced iceberg motion. *Cold Regions Science and Technology*, *15*(2), 177–190. https://doi.org/10.1016/0165-232X(88)90063-8

Massom, R. A. (1991). *Satellite remote sensing of polar regions: Applications, limitations, and data availability*. Belhaven Press in association with the Scott Polar Research Institute, University of Cambridge.

Massom, R. A., Drinkwater, M. R., & Haas, C. (1997). Winter snow cover on sea ice in the Weddell Sea. *Journal of Geophysical Research - C: Oceans*, *102*(1), 1101–1117. https://doi.org/10.1029/96jc02992

Massom, R. A., Eicken, H., Hass, C., Jeffries, M., Drinkwater, M., Sturm, M., et al. (2001). Snow on Antarctic sea ice. *Reviews of Geophysics*, *39*(3), 413–445. https://doi.org/10.1029/2000RG000085

Massom, R. A., Lytle, V. I., Worby, A. P., & Allison, I. (1998). Winter snow cover variability on East Antarctic sea ice. *Journal of Geophysical Research*, *103*(Cll), 24837–24855. https://doi.org/10.1029/98jc01617

Massom, R. A., & Stammerjohn, S. E. (2010). Antarctic sea ice change and variability – Physical and ecological implications. *Polar Science*, *4*(2), 149–186. https://doi.org/10.1016/j.polar.2010.05.001

Massom, R. A., Stammerjohn, S. E., Lefebvre, W., Harangozo, S. A., Adams, N., Scambos, T. A., et al. (2008). West Antarctic peninsula sea ice in 2005: Extreme ice compaction and ice edge retreat due to strong anomaly with respect to climate. *Journal of Geophysical Research*, *113*(C2), C02S20. https://doi.org/10.1029/2007JC004239

Melsheimer, C., & Spreen, G. (2019). AMSR2 ASI sea ice concentration data, Antarctic, version 5.4 (NetCDF). [Dataset]. PANGAEA. https://doi.org/10.1594/PANGAEA.898400

Meylan, M. H., & Bennetts, L. G. (2018). Three-dimensional time-domain scattering of waves in the marginal ice zone. *Philosophical Transactions of the Royal Society A: Mathematical, Physical & Engineering Sciences*, *376*(2129). https://doi.org/10.1098/rsta.2017.0334

Meylan, M. H., Bennetts, L. G., Cavaliere, C., Alberello, A., & Toffoli, A. (2015). Experimental and theoretical models of wave-induced flexure of a sea ice floe. *Physics of Fluids*, *27*(4), 041704. https://doi.org/10.1063/1.4916573

Meylan, M. H., Bennetts, L. G., & Kohout, A. L. (2014). In situ measurements and analysis of ocean waves in the Antarctic marginal ice zone. *Geophysical Research Letters*, *41*(14), 5046–5051. https://doi.org/10.1002/2014gl060809

Meylan, M. H., Bennetts, L. G., Mosig, J. E., Rogers, W. E., Doble, M. J., & Peter, M. A. (2018). Dispersion relations, power laws, and energy loss for waves in the marginal ice zone. *Journal of Geophysical Research: Oceans*, *123*(5), 3322–3335. https://doi.org/10.1002/2018JC013776

Meylan, M. H., & Squire, V. A. (1994). The response of ice floes to ocean waves. *Journal of Geophysical Research*, *99*(C1), 891–900. https://doi.org/10.1029/93JC02695

Meylan, M. H., Yiew, L. J., Bennetts, L. G., French, B. J., & Thomas, G. A. (2015). Surge motion of an ice floe in waves: Comparison of a theoretical and an experimental model. *Annals of Glaciology*, *56*(69), 155–159. https://doi.org/10.3189/2015AoG69A646

MIZEX Group. (1986). MIZEX East 83/84: The summer marginal ice zone program in the Fram Strait/Greenland Sea. *Eos, Transactions American Geophysical Union*, *67*(23), 513–517. https://doi.org/10.1029/EO067i023p00513

Montiel, F., Bennetts, L. G., Squire, V. A., Bonnefoy, F., & Ferrant, P. (2013). Hydroelastic response of floating elastic discs to regular waves. Part 2. Modal analysis. *Journal of Fluid Mechanics*, *723*, 629–652. https://doi.org/10.1017/jfm.2013.124

Montiel, F., Bonnefoy, F., Ferrant, P., Bennetts, L. G., Squire, V. A., & Marsault, P. (2013). Hydroelastic response of floating elastic discs to regular waves. Part 1. Wave basin experiments. *Journal of Fluid Mechanics*, *723*, 604–628. https://doi.org/10.1017/jfm.2013.123

Nelli, F., Bennetts, L. G., Skene, D. M., Monty, J. P., Lee, J. H., Meylan, M. H., & Toffoli, A. (2017). Reflection and transmission of regular water waves by a thin, floating plate. *Wave Motion*, *70*, 209–221. https://doi.org/10.1016/j.wavemoti.2016.09.003

Nelli, F., Bennetts, L. G., Skene, D. M., & Toffoli, A. (2020). Water wave transmission and energy dissipation by a floating plate in the presence of overwash. *Journal of Fluid Mechanics*, *889*, A19. https://doi.org/10.1017/jfm.2020.75

Nihashi, S., & Ohshima, K. I. (2001). Relationship between ice decay and solar heating through open water in the Antarctic sea ice zone. *Journal of Geophysical Research*, *106*(C8), 16767–16782. https://doi.org/10.1029/2000jc000399

Passerotti, G., Bennetts, L. G., von Bock und Polach, F., Alberello, A., Puolakka, O., Dolatshah, A., et al. (2022). Interactions between irregular wave fields and sea ice: A physical model for wave attenuation and ice breakup in an ice tank. *Journal of Physical Oceanography*, *52*(i), 1431–1446. https://doi.org/10.1175/JPO-D-21-0238.1

Prinsenberg, S. J., & Peterson, I. K. (2011). Observing regional-scale pack-ice decay processes with helicopter-borne sensors and moored upward-looking sonars. *Annals of Glaciology*, *52*(57 PART 1), 35–42. https://doi.org/10.3189/172756411795931688

Rice, S. O. (1945). Mathematical analysis of random noise. *The Bell System Technical Journal*, *24*(1), 46–156. https://doi.org/10.1002/j.1538-7305.1945.tb00453.x

Rothrock, D. A., & Thorndike, A. S. (1984). Measuring the sea ice floe size distribution. *Journal of Geophysical Research*, *89*(C4), 6477–6486. https://doi.org/10.1029/JC089iC04p06477

Shen, H. H., Ackley, S. F., & Hopkins, M. A. (2001). A conceptual model for pancake-ice formation in a wave field. *Annals of Glaciology*, *33*, 361–367. https://doi.org/10.3189/172756401781818239

Skene, D. M., & Bennetts, L. G. (2021). A transition-loss theory for waves reflected and transmitted by an overwashed body. *SIAM Journal on Applied Mathematics*, *81*(3), 834–852. https://doi.org/10.1137/20M1386979

Skene, D. M., Bennetts, L. G., Meylan, M. H., & Toffoli, A. (2015). Modelling water wave overwash of a thin floating plate. *Journal of Fluid Mechanics*, *777*, 1–13. https://doi.org/10.1017/jfm.2015.378

Skene, D. M., Bennetts, L. G., Wright, M., Meylan, M. H., & Maki, K. J. (2018). Water wave overwash of a step. *Journal of Fluid Mechanics*, *839*, 293–312. https://doi.org/10.1017/jfm.2017.857

Squire, V. A. (2020). Ocean wave interactions with sea ice: A reappraisal. *Annual Review of Fluid Mechanics*, *52*(1), 37–60. https://doi.org/10.1146/annurev-fluid-010719-060301

Squire, V. A., Dugan, J. P., Wadhams, P., Rottier, P. J., & Liu, A. K. (1995). Of ocean waves and sea ice. *Annual Review of Fluid Mechanics*, *27*(1), 115–168. https://doi.org/10.1146/annurev.fl.27.010195.000555

Squire, V. A., & Moore, S. C. (1980). Direct measurement of the attenuation of ocean waves by pack ice. *Nature*, *283*(5745), 365–368. https://doi.org/10.1038/283365a0

Sree, D. K. K., Law, A. W. K., & Shen, H. H. (2018). An experimental study on gravity waves through a floating viscoelastic cover. *Cold Regions Science and Technology*, *155*, 289–299. https://doi.org/10.1016/j.coldregions.2018.08.013

Sree, D. K. K., Law, A. W. K., & Shen, H. H. (2020). An experimental study of gravity waves through segmented floating viscoelastic covers. *Applied Ocean Research*, *101*(October 2019), 102233. https://doi.org/10.1016/j.apor.2020.102233

Tavakoli, S., & Babanin, A. V. (2021). Wave energy attenuation by drifting and non-drifting floating rigid plates. *Ocean Engineering*, *226*, 108717. https://doi.org/10.1016/j.oceaneng.2021.108717

Timco, G. W., & Weeks, W. F. (2010). A review of the engineering properties of sea ice. *Cold Regions Science and Technology*, *60*(2), 107–129. https://doi.org/10.1016/j.coldregions.2009.10.003

Toffoli, A., Bennetts, L. G., Meylan, M. H., Cavaliere, C., Alberello, A., Elsnab, J., & Monty, J. P. (2015). Sea ice floes dissipate the energy of steep ocean waves. *Geophysical Research Letters*, *42*(20), 8547–8554. https://doi.org/10.1002/2015GL065937

Toffoli, A., Pitt, J. P. A., Alberello, A., & Bennetts, L. G. (2022). *Modelling attenuation of irregular wave fields by artificial ice floes in the laboratory*. Philosophical Transactions of the Royal Society A. accepted. https://doi.org/10.1098/rsta.2021.0255

Toyota, T., Haas, C., & Tamura, T. (2011). Size distribution and shape properties of relatively small sea-ice floes in the Antarctic marginal ice zone in late winter. *Deep-Sea Research Part II Topical Studies in Oceanography*, *58*(9–10), 1182–1193. https://doi.org/10.1016/j.dsr2.2010.10.034

Tran-Duc, T., Meylan, M. H., Thamwattana, N., & Lamichhane, B. P. (2020). Wave interaction and overwash with a flexible plate by smoothed particle hydrodynamics. *Water (Switzerland)*, *12*(12), 3354. https://doi.org/10.3390/w12123354

Vichi, M., Eayrs, C., Alberello, A., Bekker, A., Bennetts, L. G., Holland, D., et al. (2019). Effects of an explosive polar cyclone crossing the Antarctic marginal ice zone. *Geophyical Research Letters*, *47*(11), 5948–5958. https://doi.org/10.1029/2019GL082457

Wadhams, P. (1983). A mechanism for the formation of ice edge bands. *Journal of Geophysical Research*, *88*(C5), 2813. https://doi.org/10.1029/JC088iC05p02813

Wadhams, P., Aulicino, G., Parmiggiani, F., Persson, P. O., & Holt, B. (2018). Pancake ice thickness mapping in the Beaufort Sea from wave dispersion observed in SAR imagery. *Journal of Geophysical Research: Oceans*, *123*(3), 2213–2237. https://doi.org/10.1002/2017JC013003

Wadhams, P., Lange, M. A., & Ackley, S. F. (1987). The ice thickness distribution across the Atlantic sector of the Antarctic ocean in midwinter. *Journal of Geophysical Research*, *92*(C13), 14535–14552. https://doi.org/10.1029/JC092iC13p14535

Weeks, W. F., & Ackley, S. F. (1982). *The growth, structure, and properties of sea ice* (Technical Report 82-1). U.S. Army Cold Regions Research and Engineering Laboratory.

Weeks, W. F., & Hilber, W. D. (2010). *On sea ice*. University of Alaska Press.

Worby, A. P., Jeffries, M. O., Weeks, W. F., Morris, K., & Jaña, R. (1996). The thickness distribution of sea ice and snow cover during late winter in the Bellingshausen and Amundsen Seas, Antarctica. *Journal of Geophysical Research - C: Oceans*, *101*(C12), 28441–28455. https://doi.org/10.1029/96JC02737

Yiew, L. J., Bennetts, L. G., Meylan, M. H., Thomas, G. A., & French, B. J. (2017). Wave-induced collisions of thin floating disks. *Physics of Fluids*, *29*(12), 127102. https://doi.org/10.1063/1.5003310

Yiew, L. J., Parra, S. M., Wang, D., Sree, D. K. K., Babanin, A. V., & Law, A. W. (2019). Wave attenuation and dispersion due to floating ice covers. *Applied Ocean Research*, *87*(April), 256–263. https://doi.org/10.1016/j.apor.2019.04.006

Young, I. R., Fontaine, E., Liu, Q., & Babanin, A. V. (2020). The wave climate of the Southern Ocean. *Journal of Physical Oceanography*, *50*(5), 1417–1433. https://doi.org/10.1175/jpo-d-20-0031.1